nature communications

Article

https://doi.org/10.1038/s41467-026-69244-z

Decoupling phase separation and fibrillization preserves activity of biomolecular condensates

Received: 8 April 2025

Accepted: 26 January 2026

Published online: 16 February 2026

Check for updates

Tharun Selvam Mahendran[1], Anurag Singh[2], Sukanya Srinivasan[2], Christian M. Jennings[3], Christian Neureuter[2], Bhargavi H. Gindra[2], Sapun H. Parekh[3] & Priya R. Banerjee[1,2]

The age-dependent transition of metastable, liquid-like protein condensates to amyloid fibrils is an emergent phenomenon in numerous neurodegeneration-linked protein systems. A key question is whether the thermodynamic driving forces underlying phase separation and maturation to amyloid fibrils are distinct and separable. Here, we address this question using an engineered version of microtubule-associated protein Tau, which forms biochemically-active condensates. These metastable protein condensates rapidly convert to amyloid fibrils under quiescent, cofactor-free conditions. In particular, the interfaces of condensates promote fibril nucleation, impairing condensate activity in recruiting tubulin and catalyzing microtubule assembly. Remarkably, a small molecule metabolite, L-arginine, selectively impedes age-dependent amyloid formation in a valence and chemistry-specific manner without perturbing phase separation. By enhancing condensate viscoelasticity, L-arginine counteracts the age-dependent decline in condensate activity. These results provide a proof-of-principle demonstration that small molecule metabolites can enhance the metastability of protein condensates and delay the formation of amyloid fibrils, thereby preserving biochemical function.

Protein condensation via phase separation is facilitated by an interplay between chain solvation and multivalent sequence-encoded intermolecular interactions[1–6]. Typically, protein condensates possess physical properties akin to viscoelastic fluids[7–9]. In certain protein systems associated with neurodegenerative disorders (ND), including FUS, hnRNPA1, TDP-43, and Tau, phase separation is linked to age-dependent alterations in condensate dynamics, morphology, and structure—a process known as physical aging or maturation[10–16]. The aging of protein condensates is an emergent property of the system described in recent literature using the framework of a glass transition[8], dynamical arrest of the dense phase[9], and a fluid-to-amyloid fibril transition[17]. Importantly, several clinically relevant mutations in ND-linked proteins were found to accelerate the liquid-to-fibril transition of condensates[11,12,16,18,19], indicating that protein phase separation may contribute significantly to disease-associated fibrillization[20–23]. However, an open question remains: Are the thermodynamic driving forces governing protein phase separation and fibrillization related or distinct?

Emerging experimental and computational results suggest that protein condensates are metastable relative to a globally stable solid state[9,17,24]. This may explain why stress granules hosting multiple aggregation-prone proteins become irreversible with prolonged persistence[11,25]. It is plausible that active cellular processes and molecular chaperones, previously shown to regulate protein phase behavior[26–31], could counteract the age-dependent liquid-to-solid phase transitions of biomolecular condensates. Utilizing sequence engineering approaches for the prion-like low complexity domain of hnRNPA1, it was recently shown that the physical aging of protein

[1]Department of Biological Sciences, The State University of New York at Buffalo, Buffalo, NY, USA. [2]Department of Physics, The State University of New York at Buffalo, Buffalo, NY, USA. [3]Department of Biomedical Engineering, University of Texas at Austin, Austin, TX, USA. e-mail: prbanerj@buffalo.edu

condensates is sequence-encoded and partially distinct from the interactions that drive condensate formation[24], leading to the postulate that distinct molecular grammars might exist for phase separation and physical aging. This indicates that macromolecules (such as proteins, RNAs, etc.) and/or small molecules that can selectively modulate sequence-specific interactions underlying amyloid formation could, in principle, buffer condensate liquid-to-solid transition independent of protein phase separation (Fig. 1a). Chemical targeting via small molecules has already been shown to modulate protein condensate formation and disassembly[26,32–34]. With the growing interest in targeting aberrant biomolecular condensates with small molecules[35–39], a key focus is on using small-molecule approaches to disentangle the molecular driving forces of phase separation from the physical aging of condensates associated with ND-linked proteins.

Motivated by these open questions, we sought to establish a model protein condensate system guided by the following criteria: (i) the ability to form metastable fluid-like condensates that undergo age-dependent conversion to globally stable solids under quiescent conditions, and (ii) condensates possess a tractable biochemical activity, enabling direct assessment of how physical aging affects condensate function. Establishing this benchmark will help differentiate between selectively disrupting condensate aging and broadly perturbing condensate formation, which could impact their biochemical activity. ND-linked proteins such as α-synuclein, FUS, and hnRNPA1 form condensates that undergo aging to fibrillar solids[12,15,17,40]; however, the biochemical activities of condensates formed by these protein systems have not been established yet. Conversely, the microtubule-associated protein Tau, associated with a class of NDs called Tauopathies[41–45], is known to form biochemically active condensates capable of microtubule (MT) assembly and stabilization implicated in intracellular trafficking in post-mitotic neurons[46,47]. Importantly, multiple studies have hypothesized a link between the pathological cascade of Tau and Tau condensation, as pathogenic mutations have been shown to accelerate Tau condensate maturation[48–52]. These important features provide a case for Tau as our model protein system. However, the aging of wild-type Tau condensates to amyloid fibrils is a kinetically sluggish process (Supplementary Fig. 1), hallmarked by the incredibly long timescale required for Tau aggregation and prion-like spread in vitro and in vivo[53,54]. Tau is also well known for being highly soluble and recalcitrant to aggregation in vitro, often attributed to its hydrophilic nature[44,55]. To enable Tau fibrillization within an experimentally accessible timescale, previous studies have used physicochemical perturbations, including negatively charged cofactors like heparin, shear stress, and modifications to the native protein, such as truncations or phosphorylation[49,51,56,57]. These strategies impose unintended effects on Tau condensation and their activity in MT assembly[46,58], independent of condensate aging.

Here, we use SynTag-Tau, which comprises the full-length Tau protein (2N4R isoform) and a 40-amino-acid prionogenic N-terminal tag. Serendipitously, we found that this synthetic prion-like low-complexity sequence substantially reduces the barrier to nucleation of Tau condensates into fibrils. SynTag-Tau undergoes molecular crowding-dependent phase separation in vitro to form biochemically active liquid-like condensates, similar to the untagged wild-type Tau protein[49]. Importantly, unlike the untagged protein, SynTag-Tau condensates undergo physical aging to form mesoscale amyloid fibrils in the timescale of hours under quiescent conditions and in the absence of polyanionic cofactors, shear stress, or perturbations to the core microtubule-binding domain. Using the SynTag-Tau system, we uncovered that conditions that promote protein phase separation commensurately accelerate condensate aging to amyloid fibrils. SynTag-Tau condensate interface nucleates fibril formation, yielding a disorder-to-order transition with gradual changes in the condensate's dynamical and structural properties. These age-dependent transitions in SynTag-Tau condensate physical properties accompany a progressive loss of biochemical activity in tubulin recruitment and catalyzing MT assembly. Remarkably, phase separation and physical aging in this system are decoupled by a naturally occurring small molecule metabolite abundantly present in the intracellular milieu, L-arginine (L-Arg). Our experiments show that the partitioning of L-Arg into SynTag-Tau condensates prevents age-dependent changes in the condensate microenvironment, leading to an inhibition of fibril formation. Instead, it facilitates intra-condensate percolation transitions that enhance condensate metastability. L-Arg treatment of SynTag-Tau condensates preserves their activity in MT assembly. Finally, we show that L-Arg counteracts the condensate-to-amyloid conversion of wild-type Tau similar to that of SynTag-Tau. Overall, this proof-of-principle study demonstrates that small molecule metabolites can stabilize protein condensates, preventing their transition from a liquid state to amyloid fibrils and thereby maintaining their function.

Results

Physical aging of SynTag-Tau condensates leads to the formation of ordered amyloid fibrils

Wild-type (WT) Tau form condensates in physiologically relevant buffer conditions in vitro. These condensates are biochemically active[46], but they do not transition to amyloid fibrils under quiescent conditions, thereby limiting our investigations (Supplementary Fig. 1a, b). Recent reports employing a protein sequence engineering strategy have enabled probing the interplay between phase separation and amyloid formation on an experimentally accessible timescale and resolution that is otherwise difficult to probe[59,60]. These approaches exploit the principle that in many amyloid-forming protein systems, fibril formation is constrained by high nucleation barriers, which dictate the probability and kinetics of self-assembly[61]. Inspired by this phenomenon, we sought to design a sequence-engineered variant of Tau that selectively lowers the nucleation barrier for amyloid formation while preserving its intrinsic phase separation behavior and MT assembly function. Previous reports indicate that the fibrillar self-assembly of amyloidogenic proteins can be reinforced by fusing to a compact prionogenic low-complexity sequence[62–64]. Fusion to prion-like sequences flanking an amyloid-forming protein can act as soluble entropic bristles that favor the prion-like spread of protein aggregates without directly contributing to the primary nucleation mediated by the amyloid core[65]. In the current study, we adapted the strategy of adding a prion-like low-complexity sequence as an N-terminal tag to the Tau protein (Fig. 1b). We synthesized SynTag-Tau, which consists of the full-length Tau protein (2N4R isoform) with an amino-terminal tag containing a synthetic prionogenic sequence of 40 amino acid residues[66,67] (Fig. 1b; Supplementary Fig. 2; Supplementary Table 1). The design of this specific tag is serendipitous. Alphafold3[68] predicted structure of SynTag-Tau indicates that this prion-like tag and most of the protein are intrinsically disordered, similar to that of the untagged Tau protein (Fig. 1c; Supplementary Fig. 3).

We first set out to characterize the formation and maturation of SynTag-Tau condensates utilizing a previously reported protocol of in vitro reconstitution in 10 mM HEPES (pH 7.4), 50 mM NaCl, 0.1 mM EDTA, 2 mM DTT, and a molecular crowder (10% PEG 8000)[49,52]. We tracked age-dependent morphological changes of SynTag-Tau condensates, doped with Atto488 (A488)-conjugated SynTag-Tau, by laser scanning confocal fluorescence microscopy (Fig. 1d). Within 2 to 3 hours (h or hr) after sample preparation, we observed fibrils from periphery of SynTag-Tau condensates growing in a heterogeneous manner—visible fibrils originated from some condensates but not all. The fibrils nucleated from one condensate grow into the dilute phase and attach to neighboring condensates, inducing further nucleation and propagation of fibrillar assemblies (Fig. 1d; Supplementary Video 1). This observation appears to be consistent with a recent fibril growth model in the presence of condensates[24,69], where the growth of

https://doi.org/10.1038/s41467-026-69244-z

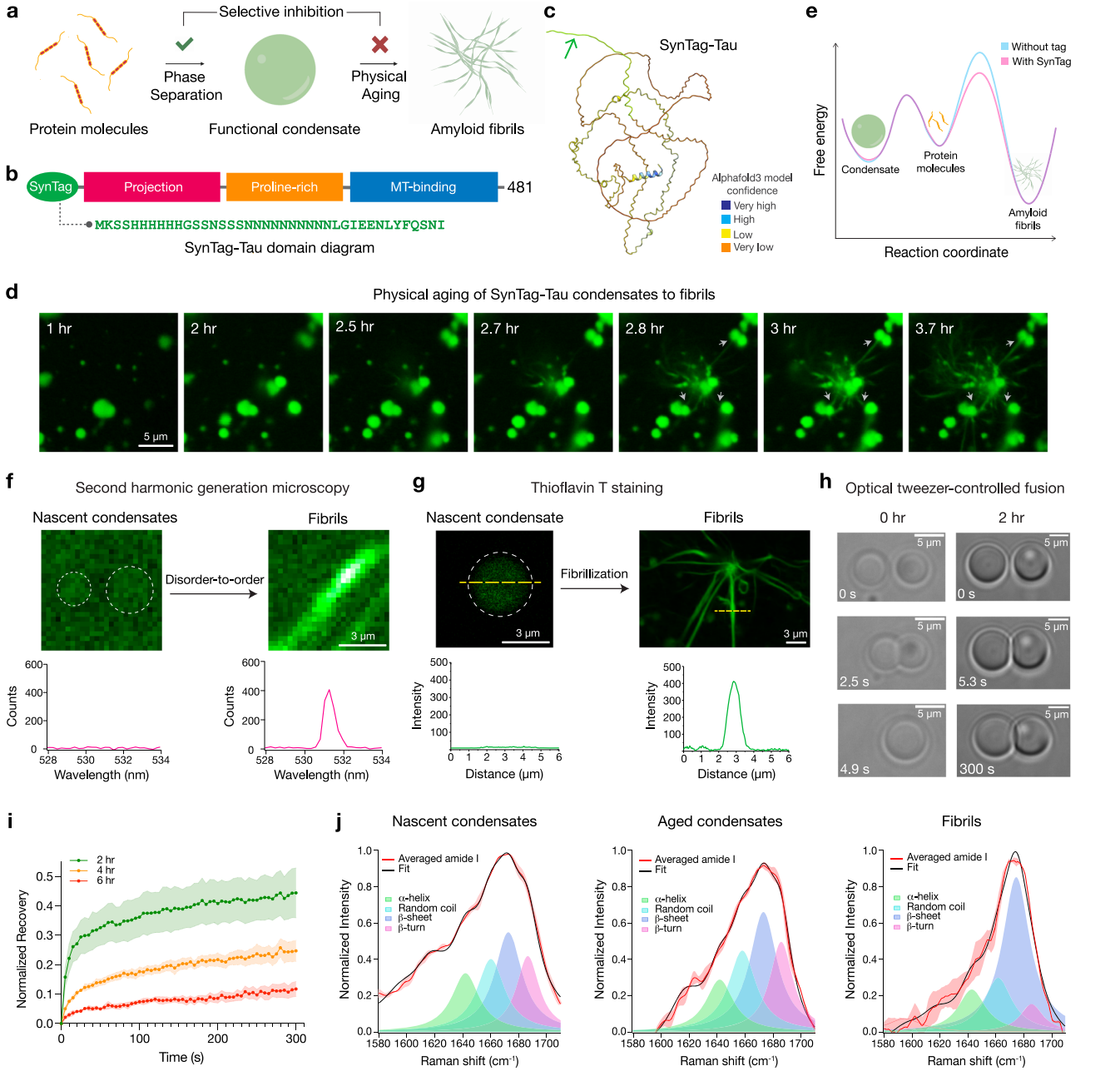

Fig. 1 | Engineered SynTag-Tau undergoes phase separation coupled to fibril formation. a Schematic depicting the formation of phase-separated protein condensates and their time-dependent transition to form amyloid fibrils. **b** Domain diagram of SynTag-Tau consisting of full-length Tau (2N4R isoform) with an N-terminal synthetic prionogenic tag (SynTag; sequence provided in green). **c** Alphafold3[68] predicted structure of SynTag-Tau. The green arrow marks the location of the tag. **d** Time-lapse imaging of Atto488-labeled SynTag-Tau condensates. Grey arrows indicate the attachment of fibrils emerging from one condensate to neighboring condensates. Also, see Supplementary Video 1. **e** Schematic of free energy landscape illustrating the relative stability of monomeric Tau, liquid-like Tau condensates, and amyloid fibrils, either with or without SynTag. **f** Second harmonic generation (SHG) microscopy shows the absence of molecular ordering in nascent SynTag-Tau condensates (indicated by dashed circles; sample age = 2 h) and the presence of spatial ordering in fibrils (sample age = 10 h). The corresponding quantification is also shown. **g** Representative Thioflavin T (ThT) fluorescence line profiles from a nascent SynTag-Tau condensate (indicated by a dashed circle; sample age = 2 h) and fibrils (sample age = 10 h). The contrast was adjusted independently in order to better visualize the nascent condensate that is very dim. **h** Optical tweezer-controlled fusion of nascent SynTag-Tau condensates (sample age = 30 mins, indicated as the 0-h time point) and condensates at 2 h of age. **i** FRAP measurements of SynTag-Tau condensates at various time points as indicated. The individual dots represent the mean value at each time point, based on data from at least three independent replicates (sample size: 2 h, 4 droplets; 4 h and 6 h, 5 droplets each). Intensity error bars were plotted based on the standard error of the mean (S.E.M.) at each time point and are represented as the shaded regions. **j** Peak fitting of averaged amide I spectra obtained from broadband coherent anti-Stokes Raman (BCARS) hyperspectral imaging shows the structural profile of SynTag-Tau in condensates at 2 h (nascent condensates) and at 6 h (aged condensates), as well as fibrils formed at 10 h of age. Spectra from multiple samples within each independent experiment ($n \geq 6$ per experiment) were averaged prior to analysis. Data are presented as mean values with S.E.M. Each experiment was independently repeated at least three times. Source data are provided as a Source Data file.

fibrils occurs in the dilute phase. Such a process engenders an efflux-generated gradient of protein molecules from nearby condensates, thereby creating a network of fibrils with condensates serving as nodes. Shuffling the primary sequence of the prionogenic tag without altering the overall sequence composition in a way that lowers the PLAAC score abrogates condensate aging to fibrils (Supplementary Fig. 4). Truncation of the tag sequence to limit it to the portion with the highest weighting in PLAAC score also renders the protein unable to trigger condensate-to-fibril transition (Supplementary Fig. 5). Thus, the specific composition and patterning of this synthetic prion-like tag sequence appear to be critical for lowering the nucleation barrier for the condensate-to-fibril conversion, assuming that the thermodynamic stability of fibrils remain unchanged (Fig. 1e). As a further validation, we sought to determine whether the SynTag could serve as the primary driver of SynTag-Tau fibril formation. ZipperDB[70] analysis revealed that in comparison to the native Tau sequence, the putative steric zippers in SynTag are outweighed in absolute score (Rosetta energy expressed as kcal/mol) and frequency, i.e., number of steric zippers (Supplementary Fig. 6). This analysis suggests that the primary steric zippers capable of driving fibril nucleation likely originate from the native Tau sequence. However, without structural studies, we cannot rule out the possibility that the putative zipper motifs in SynTag act as auxiliary steric zippers that facilitate amyloid fibril formation.

We next employed in situ second-harmonic generation (SHG), a non-linear label-free optical phenomenon ideal for probing non-centrosymmetric structures with molecular ordering[71]. We observed that SynTag-Tau fibrils, but not SynTag-Tau condensates, contain spatially ordered structures (Fig. 1f). This bears a resemblance to the SHG signal originating from bona fide amyloid fibrils observed in the brain of a transgenic model of Alzheimer's[72]. To evaluate whether these ordered fibrils nucleated by condensates are indeed enriched in cross-β-sheet structures, we employed an amyloid-sensitive dye, Thioflavin T (ThT). SynTag-Tau fibrils but not nascent SynTag-Tau condensates showed detectable ThT fluorescence (Fig. 1g). To probe the condensate-to-fibril transition in further detail, we measured the (a) timescale for droplet relaxation using a dual-trap optical tweezer, and (b) molecular mobility using fluorescence recovery after photobleaching (FRAP). We observed that the SynTag-Tau condensates undergo an age-dependent dynamical arrest, hallmarked by progressively slower condensate fusion and slower FRAP recovery, prior to the formation of visible amyloid fibrils in the mesoscale (Fig. 1h, i). At the molecular level, we hypothesized that a disorder-to-order conformational change of SynTag-Tau is likely to aid in dynamical arrest and concomitant fibrillization. To obtain an age-dependent structural fingerprint of SynTag-Tau molecules in the dense phase, we employed in situ spatially resolved broadband coherent anti-Stokes Raman scattering (BCARS)[73], which is a label-free hyperspectral Raman imaging technique. Intra-condensate BCARS measurements revealed a progressive increase in the β-sheet content with condensate age, ultimately leading to amyloid fibrils that are predominantly enriched in β-sheet conformers (Fig. 1j; Supplementary Table 2).

So far, we have established that SynTag-Tau condensates convert from a fluid-like phase to fibrils, enriched in β-sheet structures, growing in the dilute phase. Next, we asked whether these two processes are correlated, meaning how perturbing SynTag-Tau condensate formation affects SynTag-Tau fibrillization. Previous literature suggests that electrostatic interactions play a dominant role in Tau phase separation[56,74,75], which can be modulated by tuning the ionic strength of the sample buffer. We observed that increasing ionic strength diminishes SynTag-Tau phase separation (measured by condensate area fraction). Interestingly, the kinetics of SynTag-Tau fibrillization decrease in a correlated manner (Supplementary Fig. 7a, b). Further, we tested this interplay by titrating the molecular crowder concentration, wherein high [PEG 8000] favors protein phase separation propensity via depletion forces[76]. Upon increasing the concentration of the crowder, we find that SynTag-Tau phase separation is enhanced, judged by an increase in condensate area fraction, and concomitantly, the timescale for condensate-to-fibril conversion is reduced (Supplementary Fig. 7c). Taken together, these observations suggest that promoting SynTag-Tau condensation enhances fibrillization. Although the insights gained so far seemingly indicate an interplay between phase separation and fibril formation, a key question is how condensate physical aging impacts the function of SynTag-Tau condensates in tubulin recruitment and MT assembly.

Condensate physical aging impairs biochemical activity

We utilized an in vitro tubulin recruitment and MT assembly assay[46] (Fig. 2a) to quantify the impact of SynTag-Tau condensate aging on biochemical activity. We first tested tubulin partitioning in the absence of GTP, both in nascent and aged SynTag-Tau condensates. We find that the nascent condensates can recruit tubulin (labeled with HiLyte647) with homogeneous distribution throughout dense phase (Fig. 2b; Supplementary Fig. 8). Contrastingly, tubulin partitioning was attenuated in aged SynTag-Tau condensates with tubulin molecules mostly concentrating close to the interface (Fig. 2c; Supplementary Fig. 8). Next, we tested the age-dependent activity of SynTag-Tau condensates using in vitro MT polymerization assay (experimental schematic in Fig. 2a). With increasing condensate age (time = Δt), we observed a gradual reduction in MT polymerization capacity (Fig. 2d, e; Supplementary Figs. 9–11). By the 16-h time point, the ability of SynTag-Tau condensates to drive MT polymerization ceases completely. Consistently, tubulin partitioning experiments conducted using similar assay conditions as the MT polymerization assay revealed increasingly heterogeneous tubulin partitioning at later time points, which corresponds to loss of activity (Supplementary Fig. 12; Fig. 2e). The ineffective partitioning of tubulin to condensates at later ages potentially indicates that either the characteristic mesh size progressively declines with physical aging or that the fibril formation occurring at the condensate interface blocks tubulin partitioning[77,78]. Nevertheless, it is worth pointing out that at the 8-h time point, despite observing a noticeable drop in MT assembly, we do not observe a dramatic blockade of tubulin partitioning via fluorescence microscopy, which might indicate that aging-induced changes in material state, as well as perturbed tubulin binding by conformationally altered SynTag-Tau within aged condensates, might underscore condensate loss-of-activity. Overall, the loss of activity of SynTag-Tau condensates with age demonstrates that the condensate material properties affect tubulin recruitment and MT assembly. Similar attenuation of SynTag-Tau condensate activity was observed (Supplementary Fig. 13) when we increased the molecular crowder concentration from 5% to either 7.5% or 10%, which accelerates SynTag-Tau condensate-to-fibril transition (Supplementary Fig. 7c) and was previously shown to modulate condensate material properties[76].

Recent reports suggest that the interface of protein condensates plays a critical role in nucleating the liquid-to-amyloid transition[17,79,80]. This is presumed to stem from the unique conformational ensemble of the protein molecules at the condensate interface, in contrast to that in the dilute or dense phases[81]. Therefore, we asked whether SynTag-Tau condensate interfaces play a similar role in fibril formation. To address this, we employed frequency-domain fluorescence lifetime imaging (FLIM) with Atto488-labeled SynTag-Tau. FLIM is a highly sensitive imaging technique that reports on the spatial heterogeneity in the molecular microenvironment of a fluorescent probe. In our experiment, we measured the lifetime of the Atto488-labeled SynTag-Tau to interrogate the local environment of protein molecules within the condensate as they undergo age-dependent morphological transitions. We find that there is a distinct lifetime signature of SynTag-Tau

https://doi.org/10.1038/s41467-026-69244-z

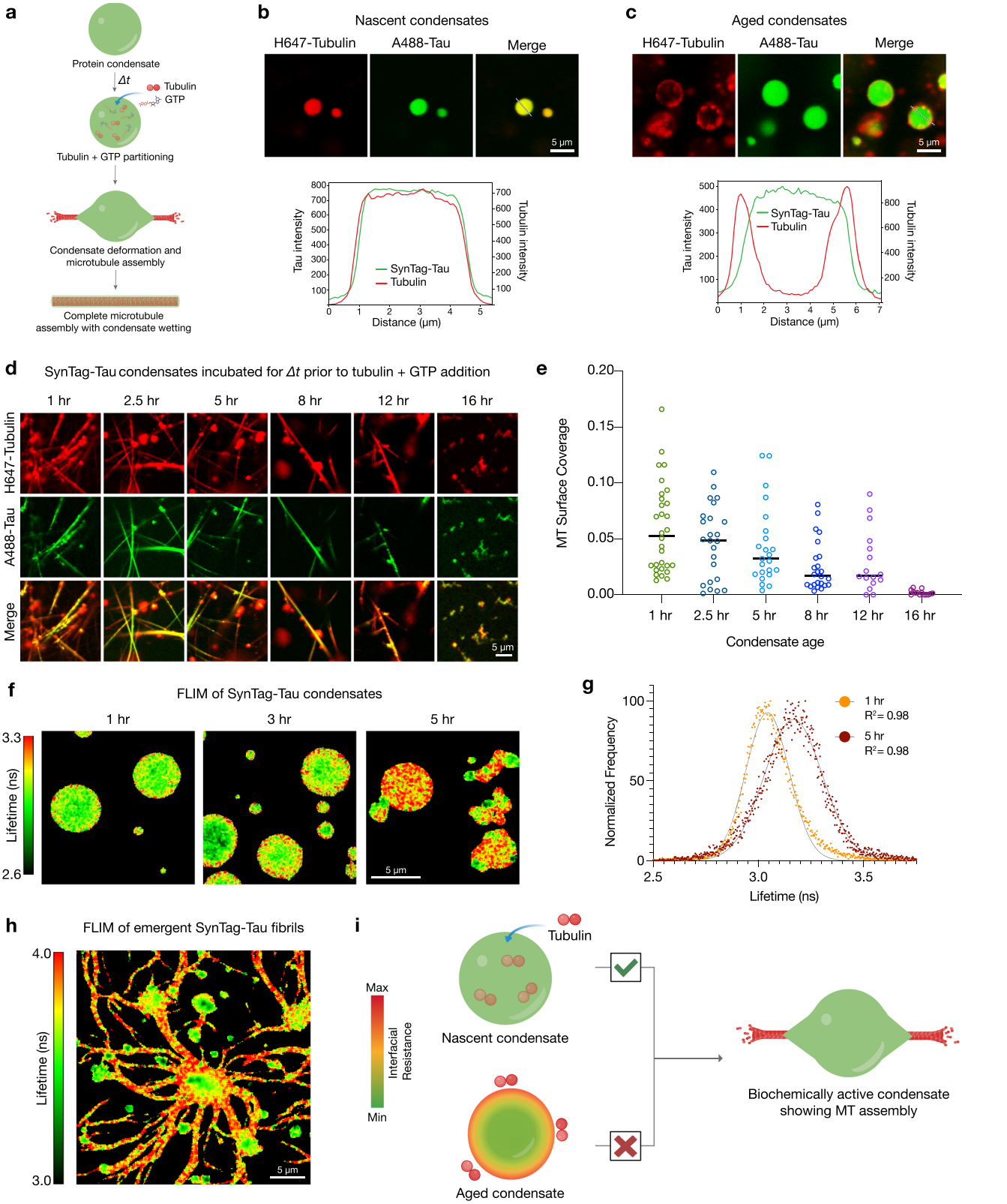

molecules on the interface of the condensates at an early age (Fig. 2f, g). The lifetimes of SynTag-Tau molecules at the condensate interface are longer than those of the interior, closer to the lifetimes of the fibrils (Fig. 2h). These data suggest that SynTag-Tau condensate interfaces nucleate amyloid formation. We infer that the altered tubulin partitioning in nascent versus aged protein condensates (Fig. 2b, c; Supplementary Fig. 12) is due to the physical aging of SynTag-Tau condensates that originates at the interface (Fig. 2i). Disabling and/or delaying the fluid-to-fibril transition of protein condensates could potentially protect against condensate loss-of-activity.

Naturally occurring small molecule metabolites modulate Tau condensate physical aging

Identifying small molecule inhibitors of protein fibrillization has been an active area of research for over two decades. In the context of phase separation, small molecules, such as 4,4′-dianilino-1,1′-

Fig. 2 | Aging transition impairs SynTag-Tau condensate activity in microtubule assembly. a Schematic of tubulin recruitment and MT polymerization in Tau condensates. **b** Nascent SynTag-Tau condensates (age = 2 h) in the presence of 50 nM HiLyte647-labeled tubulin show enrichment of tubulin in the dense phase. Corresponding line profiles are shown below. **c** Aged SynTag-Tau condensates (age = 4 h) with the addition of 50 nM HiLyte647-labeled tubulin show altered tubulin partitioning to the condensate interface. Corresponding line profiles are shown below. Display ranges in images of (b) and (c) were adjusted independently for better clarity. **d** Condensate age-dependent MT polymerization assay in SynTag-Tau condensates. **e** MT surface coverage plot corresponding to panel (d). Horizontal lines at each time point represent the median value. The individual data points represent measurements based on three independent replicates. Sample size: 1 hr, 30 datapoints; 2.5 hr, 24 datapoints; 5 hr, 23 datapoints; 8 hr, 24 datapoints; 12 hr, 16 datapoints; 16 hr, 14 datapoints. **f** Frequency-domain (FD) FLIM map of SynTag-Tau condensates at various time points. **g** Representative fluorescence lifetime distributions at 1 h and 5 h time points (since sample preparation). The points are the data, and the lines are Gaussian fittings with the corresponding goodness of fit (R^2) indicated. **h** FD-FLIM map of aged SynTag-Tau condensates with emergent amyloid fibrils (sample age = 8 h). **i** Schematic of condensate physical aging-induced interfacial resistance in SynTag-Tau condensates, and its effect on tubulin partitioning and MT assembly. Each of these experiments was independently repeated at least three times. Source data are provided as a Source Data file.

binaphthyl-5,5′-disulfonic acid (bis-ANS) and adenosine triphosphate (ATP), were shown recently to modulate the phase behavior of ND-linked proteins[26,32]. These studies and mechanistic perspectives gleaned by quantitative frameworks such as polyphasic linkage[82] and heterotypic buffering[83,84] have postulated that tuning condensate physical properties may prevent their aberrant behavior. Motivated by this perspective, we set out to test whether SynTag-Tau condensate maturation timescale can be tuned independently of SynTag-Tau phase separation through small molecule treatment. We first tested generic chemical disruptors of protein-protein interactions and naturally occurring small molecule metabolites at low millimolar concentrations. Remarkably, we found that physiologically abundant cationic amino acids, L-arginine (L-Arg) and L-lysine (L-Lys), inhibit SynTag-Tau condensate-to-fibril transition without perturbing SynTag-Tau phase separation (Fig. 3a). The concentrations at which L-Arg showed such activity are similar to its physiologically relevant concentrations[85,86]. In the presence of anionic amino acids such as L-glutamic acid (L-Glu) and L-aspartic acid (L-Asp), however, the appearance of SynTag-Tau fibrils seemed to accelerate. The observed tunability of SynTag-Tau liquid-to-fibril transition by these small molecule metabolites is likely owed to their charge and the side chain chemistry as L-proline (L-Pro), which cannot participate in electrostatic interactions, failed to show any modulatory effect (Fig. 3a). The inhibitory effect of L-Arg and L-Lys was also not recapitulated by small molecules with pleiotropic effects on protein-protein interactions, such as those that disrupt protein backbone hydrogen bonding interactions, including guanidinium hydrochloride (GnHCl) and urea (Fig. 3a). The chemical chaperone trimethylamine N-oxide (TMAO) previously reported to selectively disfavor fibril conversion of TDP-43 condensates[27] was unable to prevent SynTag-Tau phase separation coupled fibrillization (Fig. 3a). Conversely, ATP appears to hinder fibril formation, however, the condensate size and morphology are substantially affected (Fig. 3a).

We next turned our attention to L-Arg to determine its dose-dependent efficacy in perturbing SynTag-Tau fibrillization (Fig. 3b). At the lowest L-Arg concentration tested (1 mM), the partition coefficient of Atto488-labeled SynTag-Tau molecules in the dense phase is higher compared to the untreated condition. However, increasing the L-Arg concentration to 2 mM or 4 mM did not dramatically alter the partition coefficient relative to the untreated condition (Fig. 3b, c). This data suggests that SynTag-Tau phase separation is not fully inhibited by 1 mM to 4 mM L-Arg. Notably, at 2 mM L-Arg concentration, SynTag-Tau condensate size and morphology looked similar to those of the untreated condition, but the timescale of fluid-to-fibril transition shifted from 8 h to 7 days (Fig. 3b, c). At 4 mM L-Arg, however, we observed some differences in SynTag-Tau condensate size and surface wetting behavior compared to the untreated condition (Fig. 3b, c) despite the SynTag-Tau partition coefficient being largely similar. In order to ascertain whether the reduced condensate sizes stem from either altered condensate coarsening dynamics, inhibition of SynTag-Tau phase separation or both, we conducted a quantitative analysis of condensate area fraction using confocal fluorescence microscopy (Supplementary Fig. 14). We found that L-Arg concentrations of 1 mM and 2 mM yielded condensate sizes that are not significantly different than that of the untreated condition (0 mM). However, in the case of 4 mM L-Arg treatment, we observed a significantly reduced condensate area fraction, indicating that L-Arg at high concentrations (above 2 mM) inhibits SynTag-Tau phase separation and potentially affects condensate coarsening. The selective inhibition of fibrillization without abrogating condensate formation reveals a distinction in the molecular driving forces underlying these two processes, indicating that phase separation and fibrillization are biochemically separable. This decoupling phenomenon is distinct from global perturbation to condensate formation, as seen with the effect of modulating ionic strength or molecular crowding (Supplementary Fig. 7).

Next, we probed the partitioning behavior of L-Arg in SynTag-Tau condensates utilizing α-dansyl-L-arginine (dansyl-L-Arg), a fluorescent analog of L-Arg (Fig. 3d). Using dual-color fluorescence microscopy with SynTag-Tau condensates visualized with Alexa594-conjugated protein, we find favorable partitioning with a partition coefficient, k = ~4, of dansyl-L-Arg within SynTag-Tau condensates (Fig. 3e). This partition coefficient value is consistent with the known partition coefficients of similar small molecule metabolites in condensates[39]. The favorable partitioning of dansyl-L-Arg is not due to the dansyl group, as partitioning of dansyl chloride (dansyl-Cl) to SynTag-Tau condensates is markedly weaker (k = ~1.5) (Fig. 3d, e).

To investigate how the inhibitory effect of L-Arg on SynTag-Tau condensate aging is related to its chemical properties, we tested L-Arg ethyl ester (L-Arg EE) and observed no impact on SynTag-Tau condensate aging (Fig. 3f). Experiments with D-arginine (D-Arg) yielded similar results as L-Arg, revealing that the stereospecificity of arginine is not critical to its inhibitory activity (Fig. 3f). Next, we tested whether multivalent polymers of lysine or arginine as well as charged polyamines such as spermine and spermidine could impose an enhanced inhibitory potential to condensate-to-fibril transformation relative to small molecules (L-Arg/L-Lys). Intriguingly, treating condensates with multivalent cationic molecules did not offer any improvement in fibrillization timescale relative to the small molecule treatment (Supplementary Fig. 15; Fig. 3a). Given the observation that the positive hits in the small molecule screen are basic amino acids with chemical moieties of high pK_a (> 7), L-Lys (pK_a of ε-amino group = 10.5), and L-Arg (pK_a of guanidino group = 12.4), we wondered at the possibility that high pK_a could be an important chemical property that confers protection against condensate-to-fibril transition. However, the other small molecules with basic chemical moieties failed to achieve a similar effect. For example, guanidinium hydrochloride (pK_a of guanidinium group = 12.6), L-arginine ethyl ester (pK_a of guanidino group = 12.4), as well as spermine and spermidine (pK_a across multiple amine groups = ~10.7). Despite sharing highly basic, i.e., high pK_a, chemical moieties, several of these compounds failed to inhibit SynTag-Tau fibrillization selectively (Fig. 3a; Supplementary Fig. 15), which suggests that strongly basic functional groups alone are a poor predictor of inhibitory potential. Therefore, we conclude that the observed inhibitory

https://doi.org/10.1038/s41467-026-69244-z

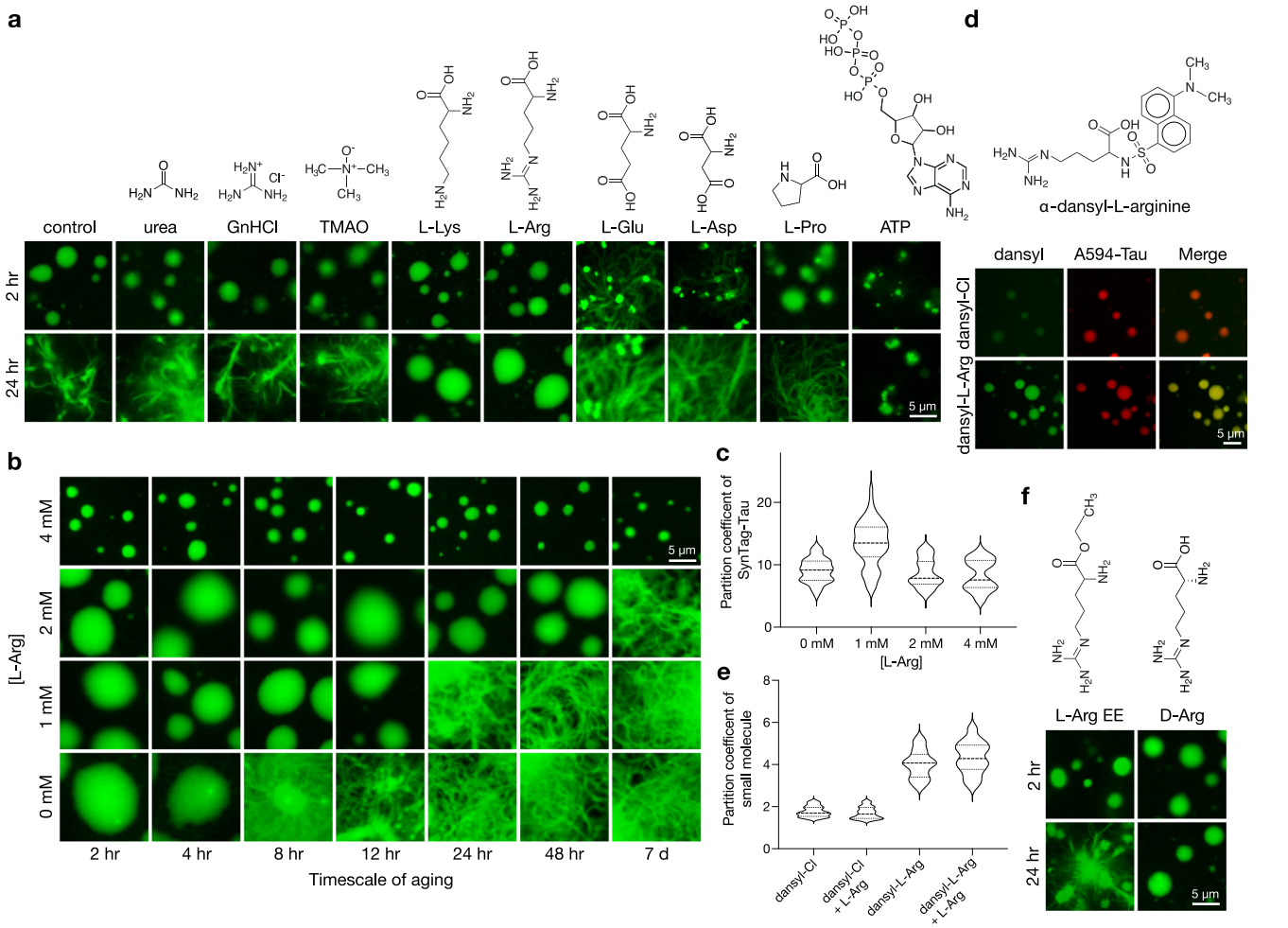

Fig. 3 | Small molecule metabolites can decouple phase separation and fibril formation in a chemistry-specific manner. a Effect of naturally occurring small molecule metabolites, chaotropic compounds, and small molecule modulators of protein-protein interactions on phase separation and fibrillization of SynTag-Tau. The chemical structure of the respective small molecule is also shown. **b** Dose-dependent effect of L-Arg in inhibition of SynTag-Tau condensate-to-amyloid transition. **c** SynTag-Tau partition coefficient analysis at different L-Arg doses. The thick dashed line of the violin plot represents the median based on data of 53 condensates from three independent replicates, whereas the thinner dotted lines above and below represent the upper and lower quartiles, respectively. **d** (top) Chemical structure of α-dansyl-L-arginine (dansyl-L-Arg). (bottom) Partitioning of either dansyl chloride (dansyl-Cl) or dansyl-L-Arg doped along with L-Arg in SynTag-Tau condensates, visualized using Alexa594- (A594) labeled SynTag-Tau, at 2 h sample age. **e** Partition coefficient analysis of either dansyl-Cl or dansyl-L-Arg, either with or without L-Arg in SynTag-Tau condensates. The thick dashed line of the violin plot represents the median based on data of 32 condensates from three independent replicates, whereas the thinner dotted lines above and below represent the upper and lower quartiles, respectively. **f** L-Arg ethyl ester (L-Arg EE), a derivative of L-Arg that lacks a carboxyl group, failed to prevent condensate aging to fibrils. D-Arginine (D-Arg) treated condensates do not transition to fibrils, similar to the L-Arg condition shown in (**a**). The display range of images shown across these figure panels was adjusted independently for better clarity. Each of these experiments was independently repeated three times. Source data are provided as a Source Data file.

activity of L-Arg at its physiological concentration is chemistry-, valence-, and charge-specific but does not depend on chirality.

L-Arg prevents cross β-sheet formation and nucleation of fibrils at the condensate interface

Given that L-Arg can prevent age-dependent changes in SynTag-Tau condensate morphology (Fig. 3), we next sought to probe its effect on the structure and dynamics of SynTag-Tau condensates. Using the ThT fluorescence assay as a function of time, we observed that the age-dependent increase in the signal originating from amyloid fibrils is notably less pronounced for condensates in the presence of L-Arg (Fig. 4a). This observation suggests that L-Arg inhibits conformational conversion of disordered SynTag-Tau molecules to cross-β-rich assemblies, preventing nucleation of amyloid fibrils. One caveat of imaging condensates at a single plane using ThT fluorescence is the lack of spatial information in the z-axis, which would be critical for resolving whether fibrils are indeed nucleated at condensate interfaces or localize to condensate interiors. We tested this by capturing z-slices and measuring A594-labeled SynTag-Tau and ThT fluorescence in untreated SynTag-Tau condensates. We find that ThT fluorescence is preferentially enriched at condensate interfaces with amyloid fibrils growing into the dilute phase, but not condensate interiors (Fig. 4b). At a relatively higher z position (0.95 μm), i.e., approaching the topmost interface of condensates (with respect to the coverslip surface), the ThT signal originating from fibrils becomes more prominent, in line with interfacial nucleation of fibrils. This is consistent with the recently proposed framework that condensate interiors could act as sinks of amyloidogenic proteins; however, their interfaces present the risk of fibril nucleation, with fibril growth occurring outward into the dilute phase[24,69]. On the other hand, L-Arg-treated SynTag-Tau condensates fail to show any notable ThT fluorescence across z-sections (Fig. 4c). For further examination, we employed BCARS hyperspectral imaging and observed that the amide I band of SynTag-Tau in nascent condensates is fairly similar in either absence or presence of L-Arg (Fig. 4d,

https://doi.org/10.1038/s41467-026-69244-z

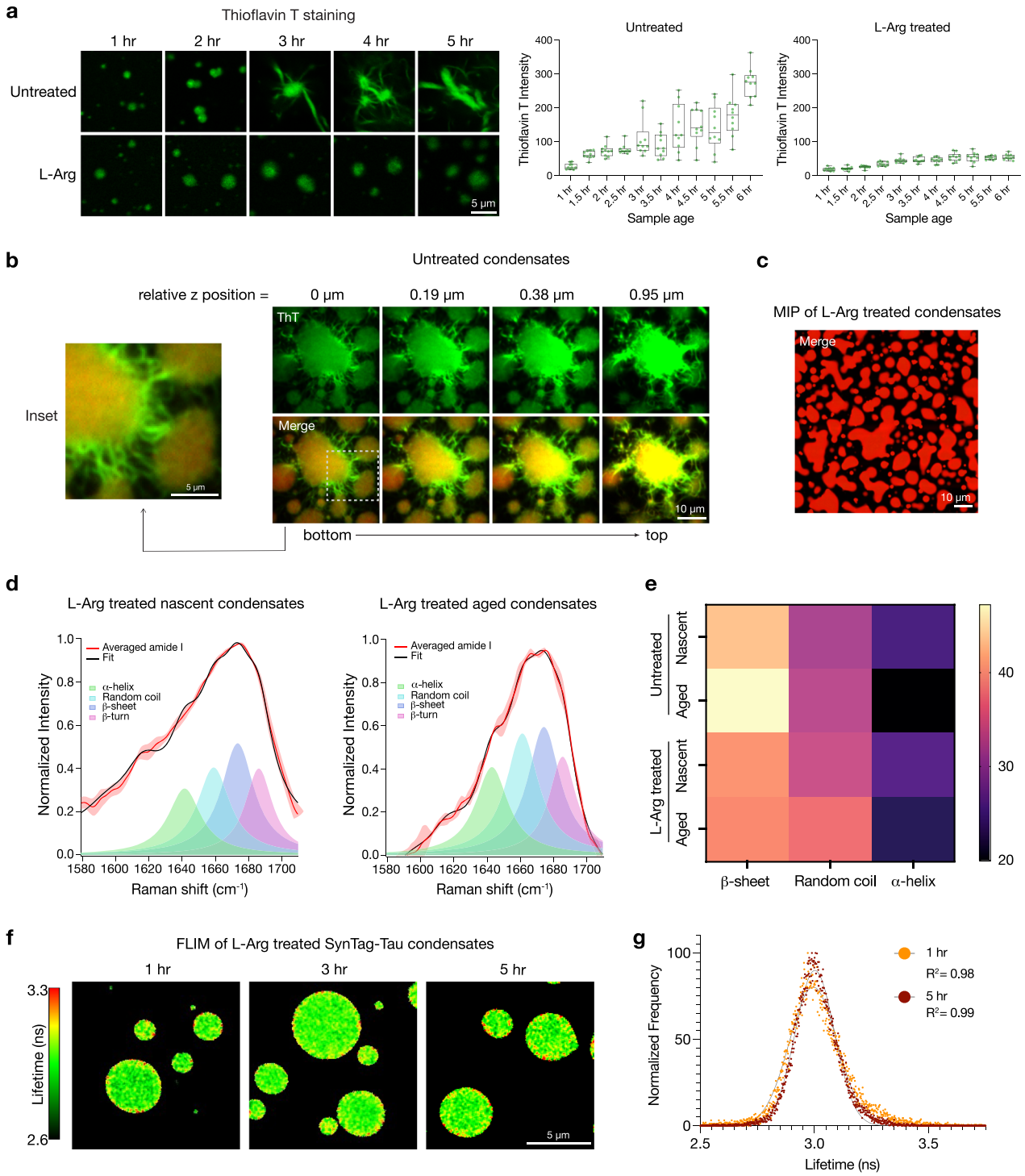

e; Supplementary Table 2). However, the amide I band of aged SynTag-Tau condensates treated with 2 mM L-Arg appears distinct from that of untreated condensates. The most dramatic difference is the decrement in the mean population of β-sheet conformers in L-Arg-treated condensates (39.3%) versus the untreated condition (47.2%). We also note a moderate increase in non-β conformations in small molecule-treated condensates relative to untreated condensates, namely random coil (37.4% vs. 32.9%, respectively) and α-helix (23.3% vs. 19.9%, respectively) (Fig. 4e). This may suggest an exciting possibility that L-Arg might slow down the SynTag-Tau condensate liquid-to-fibril conversion by populating alternative conformational states of SynTag-Tau. Follow-up work is necessary to explore this possibility further.

To probe the spatially resolved SynTag-Tau condensate microenvironment with age in the presence of L-Arg, we performed FLIM measurements using an identical approach as outlined for Fig. 2f. When comparing with the SynTag-Tau condensates without L-Arg, we made two key observations. The first is that the lifetime of fluorescently labeled SynTag-Tau molecules does not change over the same timescale, and the interface of these condensates appears similar in terms of the fluorescence lifetime with respect to the SynTag-Tau molecules at the condensate core (Fig. 4f, g). These data collectively suggest that the mesoscale changes in the SynTag-Tau condensate morphology with age are inhibited by L-Arg. Finally, we tested the efficacy of L-Arg in the heparin-induced maturation of WT Tau condensates into amyloid fibrils. L-Arg proved effective in this in vitro

https://doi.org/10.1038/s41467-026-69244-z

Fig. 4 | L-Arg prevents cross β-sheet formation and nucleation of fibrils at the condensate interface. a ThT fluorescence measurements at different sample ages, either without (untreated) or with 2 mM L-Arg. Representative images are shown on the left, and corresponding plots of ThT fluorescence intensities are shown on the right. The contrast was adjusted independently across the images to better visualize condensates and fibrils that are very dim. The center line of the box plot represents the median, and the individual data points represent 10 measurements across three independent replicates. The whiskers indicate the full range of the data from the minimum to the maximum. **b** Individual Z-slices of untreated SynTag-Tau condensates visualized using ThT (green) as well as A594-labeled SynTag-Tau (red). The indicated z-position is relative to the leftmost z-slice in the panel. The inset shown represents the area demarcated by the white-dashed box. Sample age is 96 h. **c** Maximum intensity projection (MIP) image of 2 mM L-Arg treated SynTag-Tau condensates visualized as a merge of A594-labeled SynTag-Tau and ThT fluorescence. The display range of ThT fluorescence in (**b**) and (**c**) is identical. Sample age is 96 h. **d** Peak fitting of averaged amide I spectra obtained from BCARS hyperspectral imaging of L-Arg-treated SynTag-Tau condensates reveals changes in protein molecular conformations at 2 h (nascent condensates) and 6 h (aged condensates). Spectra from multiple samples within each independent experiment ($n \geq 6$ per experiment) were averaged prior to analysis. Data are presented as mean values with S.E.M representing three independent replicates. **e** Heat map based on the amide I spectral decomposition obtained from BCARS hyperspectral imaging showing the mean percentages of protein conformations in untreated versus 2 mM L-Arg treated SynTag-Tau condensates at 2 h (nascent) and 6 h (aged) of age. The mean percentages based on measurements from three independent replicates represent the quotient of each conformation's peak fitted area divided by the cumulative area of β-sheet, random coil, and α-helix. **f** FD-FLIM map of L-Arg treated condensates at various time points (since sample preparation). **g** Representative fluorescence lifetime distributions at 1 h and 5 h time points (since sample preparation). The points are the data, and the lines are Gaussian fittings with the corresponding goodness of fit (R^2) indicated. Each of these experiments was independently repeated three times. Source data are provided as a Source Data file.

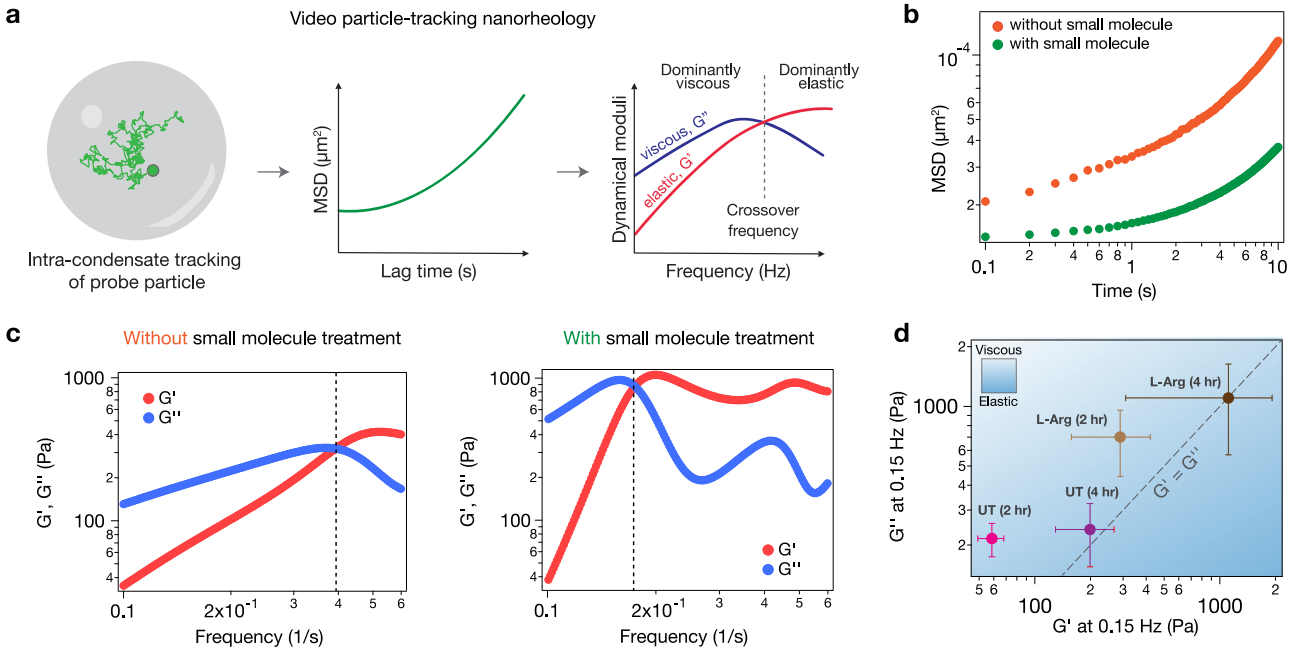

Fig. 5 | Small molecule-mediated enhancement of condensate viscoelasticity. a Schematic of video particle-tracking (VPT) nanorheology measurements using 200 nm probe particles passively embedded within Tau condensates. **b** Representative mean squared displacement (MSD) measurements of probe particles inside Tau condensates either with or without small molecule treatment (2 mM L-Arg). The measurements were conducted 2 h after sample preparation. **c** Representative dynamical moduli of Tau condensates either in the absence (left) or presence (right) of 2 mM L-Arg. The measurements were conducted 2 h after sample preparation. The dashed line represents the crossover frequency. **d** Reports a diagram-of-states for untreated (UT) and small molecule-treated (L-Arg) Tau condensates at the indicated sample age, based on the estimated moduli at 0.15 Hz. The experimentally determined data are represented as mean values with standard deviations for $n = 3$ independent replicates. The sample size for all these measurements is 3 condensates from three independent replicates. Source data are provided as a Source Data file.

model of condensate aging as well, indicating that the selective inhibitory potential of L-Arg against condensate-to-fibril transition does not stem from interactions between L-Arg and the synthetic prionogenic tag in SynTag-Tau but potentially via frustration of the interactions mediated by the zipper motifs in Tau (Supplementary Fig. 16). Contrarily, treatment with L-Glu resulted in progressively higher ThT fluorescence relative to the untreated condition, consistent with observations in the SynTag-Tau model system (Supplementary Fig. 16; Fig. 3a).

Small molecule-induced enhancement in condensate viscoelasticity weakens fibrillization propensity

The effect of L-Arg in regulating condensate-to-fibril transition may stem from modulating the material properties of Tau condensates. To test this idea, we employed video particle tracking (VPT) nanorheology using 200 nm-sized fluorescent probe particles passively embedded inside WT Tau condensates (Fig. 5a). From the mean-squared displacements (MSDs) of the fluorescent probes, we computed the frequency-dependent viscoelastic or dynamical moduli of Tau condensates. The timescale of the dominantly viscous versus dominantly elastic behavior of Tau condensates can be deduced by estimating the crossover frequency from the frequency-dependent viscoelastic moduli. In the absence of L-Arg, Tau condensates are highly viscoelastic, with probe particles exhibiting sub-diffusive motion (diffusivity coefficient, $\alpha < 1$) within the experimental timescale (Fig. 5b, c). With aging, these condensates exhibit a progressive lowering of the crossover frequency and increase in the storage (G') modulus, suggesting an enhancement in the network elasticity (Fig. 5d; Supplementary Fig. 17).

Surprisingly, L-Arg-treated condensates at 2 h of age were found to be more viscoelastic relative to that of the untreated condition (Fig. 5b, c). At 4 h, these condensates exhibit a substantial increase in viscoelasticity (Fig. 5d; Supplementary Fig. 17). These data suggest a surprising role of L-Arg in strengthening intra-condensate networking interactions, otherwise referred to as percolation[87,88]. Optical tweezer-based active fusion measurements of SynTag-Tau condensates show a consensus with nanorheology measurements (Fig. 5b **vs.** Supplementary Fig. 18a, Fig. 1h) in that L-Arg leads to a slowdown in condensate fusion speed in a dose-dependent manner. In agreement with these results, FRAP measurements at longer timescales revealed progressively slower recovery traces for L-Arg-treated condensates (Supplementary Fig. 18b). We also tested the effect of L-Glu treatment on condensate viscoelasticity (Supplementary Fig. 19). We observed that it enhances condensate viscoelasticity similarly to L-Arg; however, it is worth noting that this enhancement might stem from faster fibril assembly (Supplementary Fig. 16) rather than percolation-driven increase in the network strength. Further systematic investigation will be required to clearly distinguish these mechanisms. In total, measurements of condensate material properties reveal that L-Arg suppresses condensate-to-fibril transition via enhancement of condensate viscoelasticity.

Selective inhibition of condensate-to-fibril transition preserves condensate biochemical activity

The protective effects of L-Arg against the condensate-to-fibril conversion of SynTag-Tau motivated us to test its role in MT assembly (Fig. 2a). We observe that, similar to untreated SynTag-Tau condensates, the L-Arg-treated condensates can assemble MTs with comparable efficiency up to 5 h of physical aging (Fig. 6a, b; Supplementary Fig. 20a). After the 5-h mark, these trends start to diverge. The untreated SynTag-Tau condensates progressively lose their MT assembly activity as seen by the reduced MT formation (Fig. 2d, e). In contrast, the L-Arg-treated SynTag-Tau condensates (1 mM and 2 mM L-Arg) show a steady trend in MT assembly activity on the same timescale without appreciable decline. Particularly, at the 16-h time point, the untreated SynTag-Tau condensates completely lose activity, whereas the L-Arg-treated condensates continue to retain their function (Fig. 6a, b; Supplementary Fig. 20a). Tubulin partitioning experiments conducted under similar assay conditions revealed that L-Arg treatment is associated with homogeneous tubulin partitioning into condensates at all time points tested, which is otherwise perturbed as a function of condensate age (Supplementary Fig. 12). Moreover, FRAP measurements reveal marginally slower mobility of tubulin with L-Arg treatment, relative to the untreated condition, likely owed to the small molecule-induced enhancement in condensate viscoelasticity (Supplementary Fig. 20b; Fig. 5). Nonetheless, the outcome of MT assembly does not appear to be dramatically affected by small molecule-mediated changes in condensate material state (Fig. 6b). With our overall observations, we posit that nucleation of amyloid assemblies at the SynTag-Tau condensate interface results in the accumulation of tubulin at the condensate interface, hindering MT assembly. In the presence of L-Arg, fibril nucleation at the condensate interface is inhibited, allowing favorable partitioning of tubulin to the condensate core and facilitating tubulin polymerization (Fig. 6c).

Discussion

Previous reports have suggested that liquid-like biomolecular condensates may act as hubs for the aggregation of disease-linked proteins[20,22,89,90]. An important question in this regard is whether the driving forces for phase separation and amyloid fibril formation are the same or merely overlapping. If condensates were to be crucibles for amyloid fibril formation[91], one would speculate that physicochemical factors that stabilize the condensed phase of proteins would result in a commensurate acceleration in fibril formation. Using sequence engineering of the prion-like domain of hnRNPA1, recent reports have independently shown the separation of functions—the separability of sequence features that drive phase separation and fibril formation[17,24]. In our studies, we demonstrate an orthogonal approach to the separation-of-function paradigm by using small molecules to modulate the material properties of protein condensates. Although protein sequence engineering has been a common way to dissect the interplay between condensate formation and aging into stable solids, such approaches are not feasible to apply in disease models. Our results provide a proof-of-principle that the free energy landscape for condensate-to-fibril conversion can be selectively modulated by small molecules (Fig. 6c), thereby preserving condensate biochemical activity.

What is the mechanism of L-Arg's action in inhibiting Tau condensate-to-fibril transition? Firstly, we find that the Tau condensate interface plays a critical role in nucleating fibril formation, consistent with other protein systems that show similar aging behavior[17,79,80]. Therefore, the mechanism of L-Arg's action may rest, in part, on its ability to prevent amyloid nucleation at the Tau condensate interface, a process that leads to a crust-like solid shell formation in aged condensates[92]. Inhibition of Tau condensate interface solidification would favorably partition tubulin into the condensate core, enabling MT assembly. Secondly, L-Arg strengthens the metastable viscoelastic network of Tau condensates, thereby delaying conversion to amyloid fibrils. A similar mechanism has recently been proposed in the instance of Tau condensates treated with methylene blue[57], a long-studied drug candidate in clinical trials of Tauopathies[93]. Within the intracellular environment, L-Arg concentration is in the low millimolar range[85,86], similar to that used in our study, suggesting that L-Arg may act as a natural regulator of aberrant protein phase transitions, similar to the proposed role of ATP as a biological hydrotrope[26]. In contrast, we found that some other small molecule metabolites, such as L-Asp and L-Glu, enhance the Tau liquid-to-solid transition. These findings suggest that the cellular metabolic state itself is a critical regulator of protein phase separation and aggregation in living systems. Under diverse conditions, cells could produce a variety of metabolites that can dynamically tune the aging dynamics of biomolecular condensates.

The current study employs a unique strategy of introducing a synthetic prionogenic sequence tag to full-length Tau protein, which lowers the nucleation barrier of the condensate-to-fibril transition without perturbing condensate formation and its biochemical activity. Our findings are in corroboration with growing lines of evidence that have directly correlated the impact of disease mutations to the weakening of condensate metastability and, inversely, global stabilization of the fibrillar solid phase[12,24,94]. These observations warrant further investigations on the molecular grammars of condensate metastability and aging timescales[95]. The designed Tau protein system used in the study provided valuable insight into the effect of material properties and physical aging on condensate biochemical activity.

In summary, protein condensates are metastable fluids that must overcome a free-energy barrier to convert to fibrils, which are thermodynamically more stable (Fig. 6c). Our study reinforces the framework of the separation of functional phase separation from the age-dependent transition of condensates into irreversible solids. We experimentally demonstrated that these two processes can be decoupled by small molecules that selectively enhance condensate metastability and thereby inhibit condensate-to-amyloid transition. Our results may inspire strategies to selectively target pathological fibrillization of disease-associated proteins without perturbing their functional phase separation.

Methods

Protein purification

Codon-optimized constructs of wild-type Tau (2N4R isoform) and designed variants used in this study were synthesized and cloned into a

https://doi.org/10.1038/s41467-026-69244-z

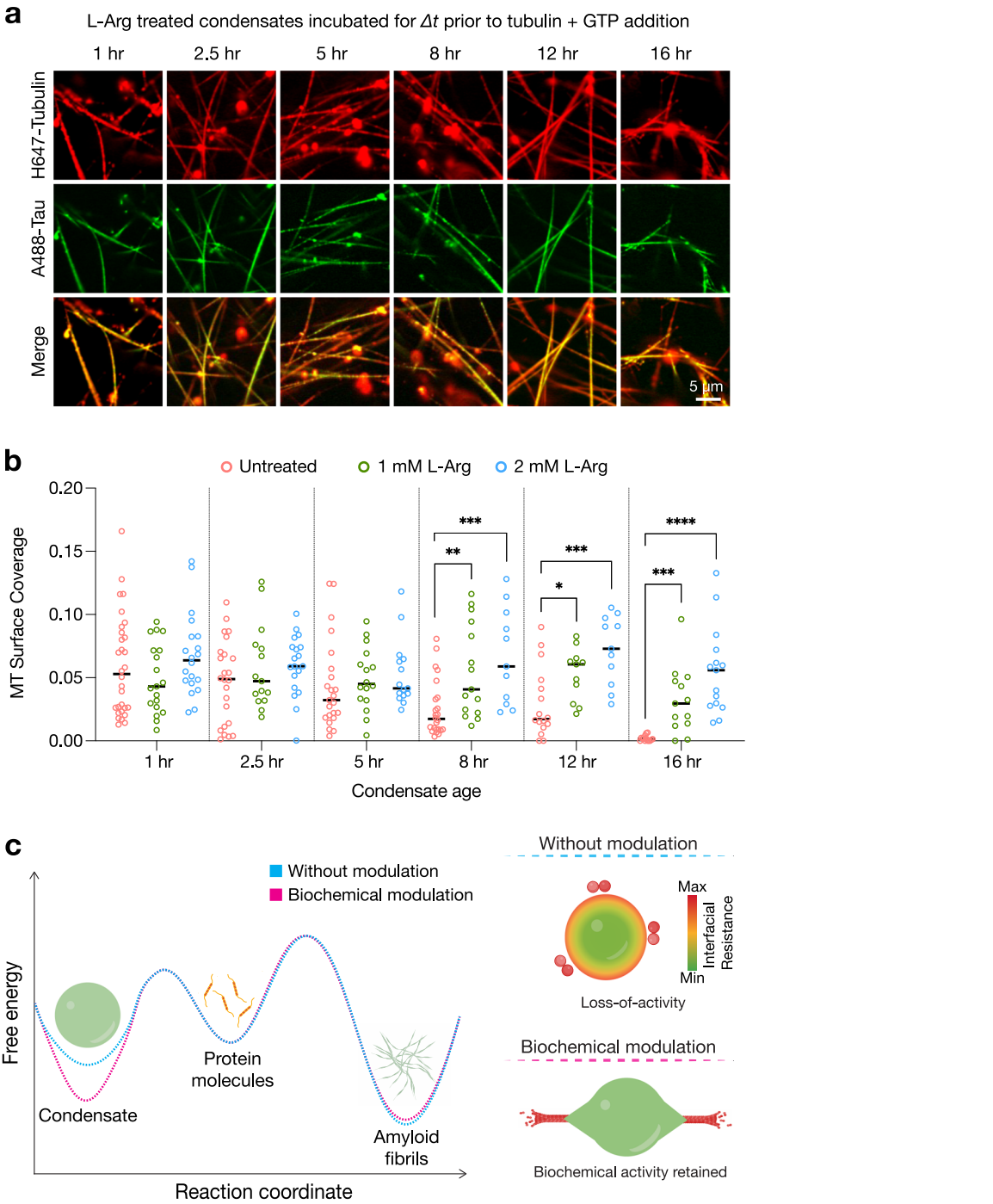

Fig. 6 | Selective inhibition of fibril formation preserves condensate biochemical activity. a MT polymerization assay of SynTag-Tau condensates treated with 1 mM L-Arg at various time points. **b** A comparison of MT surface coverage as a function of condensate age between untreated SynTag-Tau condensates (Fig. 2e) and L-Arg treated SynTag-Tau condensates (images corresponding to 2 mM condition are shown in Supplementary Fig. 20a). Horizontal black lines represent the median value. The individual data points represent measurements based on three independent replicates. Sample size for untreated condition: 1h, 30 datapoints; 2.5h, 24 datapoints; 5h, 23 datapoints; 8 h, 24 datapoints; 12 h, 16 datapoints; 16 h, 14 datapoints. For 1 mM L-Arg condition: 1h, 19 datapoints; 2.5h, 15 datapoints; 5 h, 16 datapoints; 8 h, 15 datapoints; 12 h, 11 datapoints; 16 h, 13 datapoints. For 2 mM L-Arg condition: 1 h, 20 datapoints; 2.5 h, 19 datapoints; 5 h, 15 datapoints; 8 h, 11 datapoints; 12 h, 11 datapoints; 16 h, 15 datapoints. Statistical significance was determined using an unpaired two-sided Student's *t*-test between the MT surface coverages of untreated condensates (salmon) and either 1 mM L-Arg treated condensates (green) or 2 mM L-Arg treated condensates (blue) (* means $p < 0.05$, ** means $p < 0.01$, ***means $p < 0.001$, ****means $p < 0.0001$). The associated *P* values are shown from left to right: 0.0028, 0.0003, 0.0264, 0.0006, 0.0002, and 0.00009. **c** Schematic representing the proposed model of biochemical modulation of condensate metastability governing protein condensate-to-fibril conversion and its impact on the condensate biochemical activity in tubulin partitioning (shown as dimers) and MT formation (shown as tubule). These experiments were independently repeated three times. Source data are provided as a Source Data file.

pET His6 N10 TEV LIC vector by GenScript. SynTag-Tau protein was expressed and purified under denaturing conditions from the E. coli BL21 strain (New England Biolabs). Initially, E. coli cells were grown to OD_{600} of 0.6–0.8 and subsequently induced with 0.1 mM IPTG at 37 °C for 2 h. After pelleting, the cells were resuspended in a lysis buffer composed of 50 mM phosphate buffer (pH 6.4), 1 M KCl, 10 mM imidazole, 2 mM DTT, 6 M urea, and a protease inhibitor cocktail (Thermo Fisher Scientific). The resuspended lysate solution was subject to ultrasonication followed by ultracentrifugation at 37,500 × *g* for 30 mins at 30 °C. The extracted supernatant from the previous step was introduced to a packed Ni-NTA column at 4 °C (5 ml volume; Thermo Fisher Scientific) prewashed with the lysis buffer. After several washing steps, the proteins were eluted from the column using an elution buffer composed of 50 mM phosphate buffer (pH 6.4), 2 M KCl, 200 mM imidazole, 2 mM DTT, and 3 M urea. The elutes were pooled and introduced to a pre-equilibrated Zeba spin desalting column (Thermo Fisher Scientific) following the manufacturer's instructions to get rid of residual imidazole and for storage in a buffer composed of 50 mM phosphate buffer (pH 6.4), 2 M NaCl, 2 mM DTT, and 3 M urea. This step was repeated twice to ensure efficient desalting. The resulting protein stock was tested for nucleic acid contamination, and the protein concentration was estimated by a NanoDrop 1 C spectrophotometer.

In the case of wild-type (WT) Tau (2N4R isoform) with 6xHis tag, the protein was expressed and purified under native conditions from the E. coli BL21 strain (New England Biolabs). Initially, E. coli cells were grown to OD_{600} of 0.6–0.8 and subsequently induced with 0.1 mM IPTG at 37 °C for 2.5 h. After pelleting, the cells were resuspended in a lysis buffer composed of 50 mM MES (pH 6.0), 300 mM NaCl, 10 mM imidazole, 2 mM DTT, 1 mM EDTA, 1 mM phenylmethylsulfonyl fluoride (PMSF, Sigma Aldrich), and a protease inhibitor cocktail (Thermo Fisher Scientific). The resuspended lysate solution was subject to ultrasonication followed by ultracentrifugation at 37,500 × g for 30 mins at 4 °C. The extracted supernatant was then incubated with Ni-NTA resin (pre-equilibrated with the lysis buffer) overnight at 4 °C (5 ml volume; Thermo Fisher Scientific). The protein was eluted from the Ni-column after several wash steps using an elution buffer composed of 50 mM MES (pH 6.0), 300 mM NaCl, 250 mM imidazole, 2 mM DTT, 1 mM EDTA, and 0.3 mM PMSF. Protein fractions containing 6xHis-tagged Tau protein were incubated with TurboTEV protease (Eton Bioscience) overnight at 4 °C. The proteolysis reaction volume was loaded onto another Ni-column to remove the free 6xHis tag, non-cleaved protein, and TEV protease. The supernatant containing unbound Tau protein was diluted in a buffer containing 50 mM MES (pH 6.0), and 2 mM DTT and then loaded onto a Capto HiRes S 5/50 cation exchange column (Cytiva) for ion-exchange chromatography. Tau protein was eluted from the column by a step gradient of 0 to 1 M NaCl. Purified protein in storage buffer containing 50 mM MES (pH 6.0), 500 mM NaCl, and 2 mM DTT was tested for nucleic acid contamination, and the protein concentration was estimated by a NanoDrop 1 C spectrophotometer.

Finally, SDS-PAGE analysis was conducted to test the quality of all the purified proteins prior to flash-freezing the protein aliquots and storage at −80 °C. Site-specific fluorescence labeling of proteins was accomplished following the manufacturer's instructions. For the sequence details of WT and other Tau variants used in this study, refer to Supplementary Table 1.

Preparation of protein condensate samples

After thawing an aliquot of purified Tau protein at room temperature, desalting was conducted using an equilibrated Zeba spin desalting column (Thermo Fisher Scientific), following the manufacturer's instructions, using a buffer composed of 10 mM HEPES (pH 7.4), 200 mM NaCl, 0.1 mM EDTA, and 2 mM DTT. The choice of this buffer composition for a majority of the experiments reported in our study is based on the observation that it provides conditions for favorable protein phase separation into large condensate sizes that are amenable to quantitative experimental interrogation, and for clear demarcation of condensate interface from their interior (Supplementary Fig. 7). The previous step was repeated twice to ensure efficient desalting. The resulting protein was concentrated, and its concentration was measured using a NanoDrop 1 C spectrophotometer. The final sample for experiments was then prepared by diluting the concentrated protein solution in the same buffer without NaCl. Next, PEG 8000 (Sigma Aldrich) was added at a desired concentration (specified in the figure legends and this Method section) to trigger phase separation. Whenever applicable, small molecules were introduced into the sample buffer during the protein dilution step. Small molecules, including L-arginine, D-arginine, L-arginine ethyl ester, L-lysine, L-proline, L-aspartic acid, L-glutamic acid, adenosine triphosphate, α-dansyl-L-arginine, dansyl chloride, GTP, and trimethylamine N-oxide, were procured from Sigma Aldrich; urea and guanidinium hydrochloride were procured from Thermo Fisher Scientific. Many of the small molecule stocks were prepared with water, except for dansyl chloride and α-dansyl-L-arginine, which were dissolved in water spiked with DMSO; the final concentration of DMSO in condensate samples is less than 1%. Multivalent polymers/polyamines such as penta-lysine, deca-lysine, and deca-arginine were procured from GenScript, whereas spermine and spermidine were procured from Sigma Aldrich. The stocks of these multivalent molecules were prepared in water and introduced into the sample buffer, similar to the small molecules. In Thioflavin T (ThT; Thermo Fisher Scientific) based experiments, ThT at a final concentration of 50 μM was introduced during the protein dilution step. Pipetting was carried out subsequently to ensure sufficient mixing of all components in the sample to form protein condensates. The final sample was sandwiched between a tween 20-coated coverslip and a glass slide, separated by three layers of double-sided tape. The remaining space was filled with mineral oil to seal the sample chamber and prevent evaporation. Fluorescence imaging was performed either using a Q2 laser scanning confocal microscope (ISS Inc., 63× objective), a Lumicks (60× objective) C-trap confocal microscope, or a Zeiss LSM710 (63× objective) confocal microscope. An Andor Dragonfly 600 confocal platform (Oxford Instruments), equipped with an Andor iXon Ultra EMCCD camera and a Leica HC PL APO 63x/1.40-0.60 oil objective, was used for generating z-stack fluorescence images.

The preparation of wild-type Tau condensates was carried out similarly to that of SynTag-Tau and related variants, with the exception of including 6.25 μM heparin (Santa Cruz Biotechnology) in the sample buffer (unless specified otherwise) prior to induction of phase separation by the addition of PEG 8000. The sample was then placed inside an incubator set at 37 °C. These conditions were shown previously to enhance the physical aging of Tau condensates[57].

The experimental conditions relevant to the data shown in Fig. 1 are as follows. For Fig. 1d, the concentration of SynTag-Tau used is 24 μM with 10% PEG 8000. For Fig. 1f, g, j, the concentration of SynTag-Tau used is 12 μM with 10% PEG 8000. For Fig. 1h, i, the concentration of SynTag-Tau used is 12 μM with 7.5% PEG 8000. The buffer composition in all samples here is 10 mM HEPES (pH 7.4), 50 mM NaCl, 0.1 mM EDTA, and 2 mM DTT. Wherever applicable, the concentration of Atto488-labeled SynTag-Tau is 250 nM, and the concentration of ThT is 50 μM. The experimental conditions relevant to the data shown in Fig. 2 are as follows. The concentration of SynTag-Tau protein used in Fig. 2b, c is 24 μM with the following buffer composition, 10 mM HEPES (pH 7.4), 50 mM NaCl, 0.1 mM EDTA, and 2 mM DTT, along with 10% PEG 8000. The concentration of HiLyte647-labeled tubulin is 50 nM. In Fig. 2f–h, the concentration of SynTag-Tau protein is 12 μM with the same buffer composition as Fig. 2b, c. In Fig. 2d, the concentration of SynTag-Tau used is 12 μM with the following buffer composition, 80 mM PIPES (pH 6.9), 2 mM $MgCl_2$, 0.5 mM EGTA, and 2 mM DTT,

along with 5% PEG 8000. In Fig. 2d, the tubulin concentration is 5 μM, and the concentration of GTP is 1 mM. Wherever applicable, the concentrations of Atto488-labeled SynTag-Tau and HiLyte647-labeled tubulin are 250 nM and 500 nM (unless specified otherwise), respectively. The experimental conditions relevant to the data shown in Fig. 3 are as follows. The composition of these samples is 12 μM SynTag-Tau in buffer containing 10 mM HEPES (pH 7.4), 50 mM NaCl, 0.1 mM EDTA, and 2 mM DTT along with 7.5% PEG 8000. Small molecules were introduced prior to the induction of protein phase separation, and their concentrations used in these experiments are 2 mM unless specified otherwise. Wherever applicable, the concentration of Atto488-/Alexa594-labeled SynTag-Tau is 250 nM, and the concentration of dansyl-L-Arg/dansyl-Cl is 500 nM (doped either with or without L-Arg to make up a total small molecule concentration of 2 mM). The experimental conditions relevant to the data shown in Fig. 4 are as follows. The composition of these samples is 12 μM SynTag-Tau in buffer containing 10 mM HEPES (pH 7.4), 50 mM NaCl, 0.1 mM EDTA, and 2 mM DTT, along with 10% PEG 8000 crowder. The L-Arg concentration used in these experiments is 2 mM. Wherever applicable, the concentration of A488/A594 labeled SynTag-Tau is 250 nM, and the concentration of ThT is 50 μM. The experimental conditions relevant to the data shown in Fig. 5 are as follows. The composition of the samples used here is 40 μM Tau in buffer containing 10 mM HEPES (pH 7.4), 50 mM NaCl, 0.1 mM EDTA, and 2 mM DTT, along with 7.5% PEG 8000, and 6.25 μM heparin. Wherever applicable, the L-Arg concentration used in experiments is 2 mM. The experimental conditions relevant to the data shown in Fig. 6 are as follows. The composition of the samples used here is 12 μM SynTag-Tau protein in buffer containing 80 mM PIPES (pH 6.9), 2 mM $MgCl_2$, 0.5 mM EGTA, and 2 mM DTT, along with 5% PEG 8000 crowder. The tubulin concentration used here is 5 μM, and the concentration of GTP is 1 mM. The concentrations of Atto488-labeled SynTag-Tau and HiLyte647-labeled tubulin are 250 nM and 500 nM, respectively. The L-Arg concentration used in the small molecule-treated conditions is either 1 or 2 mM (indicated in the figure legends). Other details of the samples can be found in the respective figure legends or in the Methods.

Fluorescence recovery after photobleaching (FRAP)

Protein condensate samples placed on a Tween 20-coated sample chamber were kept on a confocal microscope stage (Lumicks C-trap) and imaged with a 60× water immersion objective of 1.3 numerical aperture. Imaging steps of either Atto488-labeled SynTag-Tau or HiLyte647-labeled tubulin were accomplished using the respective excitation laser line. Selection of the region of interest (ROI) for reference, bleaching, and continuous imaging for monitoring fluorescence recovery was done using the Bluelake software (Lumicks). The bleaching ROI dimensions were kept consistent for all condensate samples. Each condensate sample was bleached for at least 5 frames at maximum laser power to achieve optimal bleach depth, with a dwell time of 150 ms per pixel. Recovery of fluorescence was recorded for a maximum of 300 seconds after the bleaching steps. The images from the FRAP experiments were analyzed using Fiji[96] (version 1.54 f) to quantify the fluorescence recovery as a function of time. The intensities were normalized and corrected as described previously[97]. Succinctly, the normalization accounts for a correction for background intensity after the bleaching step as well as the photo-fading that follows, using the following expression, wherein $I_{correct}(t)$ is the intensity of the bleached ROI at time t corrected for photofading and $I_{correct}(0)$ is the value of intensity before the start of the bleach step (reference ROI used for quantifying the bleaching depth):

$$I_{normalized}(t) = \frac{I_{correct}(t) - \min(I_{correct})}{I_{correct}(0) - \min(I_{correct})} \quad (1)$$

In total, 4 to 6 fluorescence recovery traces representative of three independent replicates were gathered and averaged.

Second-harmonic generation (SHG) imaging

SHG measurements were made using a Nd:YAG microchip laser generating nanosecond pulses with a repetition rate of approximately 1 MHz at 1064 nm (Leukos Opera HP, Leukos). A 100×, 0.85 NA objective (LCPLN100XIR, Olympus) focused the beam to the sample plane, and the transmission SHG signal was collected with a 20×, 0.4 NA objective (M-20X, MKS Newport). The signal was measured with a spectrometer (IsoPlane 160, Teledyne Princeton Instruments) and a back-illuminated, deep-depletion CCD (Blaze 1340 ×400 HS, Teledyne Princeton Instruments). The CCD integration time per pixel was 1000 ms. Samples were stage-scanned with a pixel spacing of 0.3 μm per pixel.

Optical tweezer-mediated coalescence assay

Optical trap-induced fusion of protein condensates was accomplished using a Lumicks C-trap optical tweezer system equipped with a dual trap and a laser scanning confocal fluorescence microscope, with a 60x water immersion objective of numerical aperture 1.3, following a protocol described previously[98,99]. In brief, for a typical condensate fusion experiment, two condensates were trapped using a 1064 nm laser with the minimum power setting (~100 μW) to minimize laser-induced heating effects. Typically, the 1064 nm laser used in the assay provides a power of 1 mW at the objective (measured at the exit of the laser light from the objective). For the experiments, a power of 10% of 1 mW, which corresponds to ~100 μW, was used. This power is sufficient to trap droplets using the dual-trap optical tweezer system and perform droplet fusion assays[98]. The trapping of condensates relies on the refractive index mismatch between the condensate dense phase and the surrounding dilute phase. After trapping, Trap 2 was kept fixed, and Trap 1 was moved towards Trap 2 at a constant velocity of 100 nm/s. The trap is set to maintain this velocity until the fusion process concludes, allowing the final droplet to relax to a spherical or equilibrium shape. A bright-field camera was used to take time-lapse images of the droplet fusion event at 15 frames per second.

Broadband coherent anti-Stokes Raman (BCARS) hyperspectral imaging

For structural analysis of SynTag-Tau conformers within condensates or fibrils, we used an in-house-built, broadband coherent anti-Stokes Raman scattering microscope. For excitation, a Nd:YAG microchip laser generates nanosecond pulses with a repetition rate of approximately 1 MHz at 1064 nm and a broadband supercontinuum that ranges from 1100 – 2400 nm (Leukos Opera HP, Leukos). The beams were focused on the sample plane via a 100×, 0.85 NA objective (LCPLN100XIR, Olympus). In a transmission configuration, the signal was collected with a 20×, 0.4 NA objective (M-20X, MKS Newport). The signal was measured with a spectrometer (IsoPlane 160, Teledyne Princeton Instruments) and a back-illuminated, deep-depletion CCD (Blaze 1340 ×400 HS, Teledyne Princeton Instruments). Curve-fitting measurements were performed by scanning the sample with a pixel spacing of 0.4 μm. The integration time per pixel was 80-150 ms to maximize the signal without saturating the CCD.

BCARS data processing

As reported in previous studies, raw BCARS spectra were transformed into Raman-like spectra for quantitative analysis using a modified Kramers–Kronig transform for phase retrieval[100,101]. Then, a second-order Savitzky-Golay with a 151-point (approximately Δ492 cm^{-1}) smoothing window was applied to the phase-retrieved spectra to produce the Raman-like spectra.

An average spectrum for phase-separated condensates was extracted using a 3×3 pixel mean. Fibril average spectra were

calculated as the mean spectra within a drawn region of interest around the fibril. The average Raman-like spectra were subsequently normalized by the max spectral intensity[102] arising from the CH3 vibration located at 2933.4 cm^{-1}. BCARS post-processing is performed in Igor Pro 8.4 (WaveMetrics). For consistency, center wavelength dependencies of the spectrometer calibration required a spectral shift of less than or equal to 10 cm^{-1} before amide I curve-fitting. A Gaussian peak was fit to the CH3 peak to identify the center of the CH3 peak. Seven spectral points were linearly interpolated between each measured wavenumber, and the entire spectra shifted by the difference between the CH3 center and 2933.4 cm^{-1}.

Amide I decomposition was performed with Igor Pro MultiPeak Fitting 2 functionality, which employs an iterative Levenberg–Marquardt algorithm. The parameters of the Lorentzian peaks for curve-fitting are found in Supplementary Table 2. Briefly, we used six peaks[73,103,104] within the amide I band (1550 – 1725 cm^{-1}): 1644 cm^{-1} for α-helices, 1660 cm^{-1} for random coils, 1673 cm^{-1} for β-sheets, a minor peak for β-turns at 1691 cm^{-1}, and two minor peaks for tyrosine ring modes at 1600 cm^{-1} and 1612 cm^{-1}.

Tubulin partitioning and microtubule assembly functional assay

Tubulin and HiLyte647-labeled tubulin were purchased from Cytoskeleton. Partitioning experiments, using HiLyte647-labeled tubulin, were conducted on condensate samples composed of SynTag-Tau protein at 24 µM protein concentration with a PEG 8000 concentration of 10% with the following buffer composition: 10 mM HEPES (pH 7.4), 50 mM NaCl, 0.1 mM EDTA, and 2 mM DTT. The HiLyte647-labeled tubulin was introduced to SynTag-Tau condensates that were allowed to incubate within a microfuge tube for a defined period (as indicated in the text). The concentration of HiLyte647-labeled tubulin is specified in the text. In addition, the partitioning experiments were also performed under sample conditions corresponding to the microtubule polymerization assay (described below). The microtubule polymerization assay was carried out based on methods described previously[46,58]. For a schematic of the assay, refer to Fig. 2a. Briefly, SynTag-Tau protein solution was buffer-exchanged to general tubulin buffer (Cytoskeleton) consisting of 80 mM PIPES (pH 6.9), 2 mM $MgCl_2$, and 0.5 mM EGTA, supplemented with 2 mM DTT. This buffer composition was specifically used for this assay, as it was shown to support robust and reproducible tubulin polymerization under near-physiological conditions[52]. The addition of PEG 8000 to the buffer-exchanged sample at a final concentration of 5% induced the formation of protein condensates. These condensates are allowed to incubate within a microfuge tube for a defined period, as mentioned in the text, before the addition of tubulin and GTP at final concentrations of 5 µM and 1 mM, respectively. 500 nM HiLyte647-labeled tubulin was doped along with unlabeled tubulin for MT polymerization assays. Finally, the sample was prepared for fluorescence microscopy as described in the '*Preparation of protein condensate samples*' method section, with imaging conducted after a sample incubation period of 30 minutes.

Image analysis to estimate microtubule surface coverage

The analysis of microtubule surface coverage was performed using a custom-made Python-based image analysis program. Initially, raw images were loaded into the analysis program and subjected to median filtering to suppress noise, followed by Richardson-Lucy deconvolution to enhance the resolution and clarity. To further accentuate these structures, gray-scale dilation and erosion were applied alongside contrast stretching and Gabor filtering, which specifically highlighted the microtubular objects in the image. Following enhancement, the brightest objects, predominantly condensates, were isolated through an intensity threshold. These objects were then removed using binary morphological operations combined with region labeling, where the eccentricity of each region was calculated to differentiate spherical condensates from microtubule structures. After excluding the condensates, the processed images were subjected to another round of thresholding to selectively identify microtubules. This selection was refined by assessing the eccentricity of dimmer blobs, which were likely overlooked in the initial removal step. Such blobs were excluded to avoid falsely conflating condensates with the microtubule structures. Final mask refinement involved additional binary morphological operations to fine-tune the segmentation. The resulting microtubule mask was then measured quantitatively. The final mask was measured, and data, including an overlay image and a data frame of measurements, such as microtubular coverage, were exported for further analysis (Supplementary Fig. 11).

Frequency-domain fluorescence lifetime imaging (FD-FLIM)

FD-FLIM measurements of protein condensate samples were collected using a Q2 laser scanning confocal microscope (ISS Inc.) equipped with FastFLIM modules[105]. For calibration prior to FLIM measurements, Rhodamine110 dye diluted in water, with a fluorescence lifetime of 4.0 ns, was used. The fitting of the phase delay and modulation ratio of the acquired FD-FLIM data of a given condensate sample at digital modulation frequencies ranging from 20 to 100 MHz was used to estimate the fluorescence lifetime distribution of Atto488-labeled SynTag-Tau. Subsequently, this was used to map the distribution of fluorescence lifetimes in the condensate images. Generation of the corresponding fluorescence lifetime histograms of condensate samples at different imaging time points, as well as thresholding, was carried out using the ISS VistaVision software. Gaussian fitting of the fluorescence lifetime histograms was accomplished using GraphPad Prism 10.

Image analysis for estimating partition coefficient

Condensate samples used for partition coefficient analysis were imaged either using a Lumicks C-trap confocal microscope (60×) or a Zeiss LSM710 confocal microscope (63×). For each set of experiments, the microscope used and the acquisition settings were kept consistent. The concentration of labeled proteins/molecules, as well as the settings used for the respective excitation laser lines, was kept consistent across samples. Fluorescence images collected for partition coefficient image analysis were analyzed using Fiji[96] to segment individual condensates and estimate the mean intensity of each condensate (dense phase), referred to as I_{dense}. To estimate the background mean fluorescence intensity (dilute phase) referred to as I_{dilute}, three regions away from the condensates were selected at random. The partition coefficient (k) is finally estimated by dividing the dense phase mean intensity and the dilute phase mean intensity, $k = I_{dense}/ I_{dilute}$.

Estimation of Thioflavin T (ThT) fluorescence intensity

Condensate samples were prepared following a protocol as outlined in the '*Preparation of protein condensate samples*' method section. The samples were imaged either using a Lumicks C-Trap confocal microscope or an ISS Q2 laser scanning confocal microscope, wherein, for each set of experiments, the microscope used and the acquisition settings were kept consistent. The acquired fluorescence images were quantified using Fiji to estimate the mean ThT fluorescence intensity, with correction for the background ThT fluorescence intensity. These ThT measurements were performed either in the absence or presence of a small molecule to assess whether the small molecule treatment leads to enhanced or reduced fibril formation kinetics using ThT fluorescence intensity as a proxy.

Video particle tracking (VPT) based nanorheology

VPT-based nanorheology measurements were conducted on wild-type Tau condensates following the protocol outlined in a previous report[84]. In brief, we utilized 200 nanometer-sized carboxylate-modified polystyrene beads (yellow-green fluorescent tracers; FluoSpheres™, Invitrogen) introduced into the sample buffer

(0.0005 % solids) prior to induction of Tau phase separation, along with heparin. The remainder of the sample preparation was carried out as prescribed in the '*Preparation of protein condensate samples*' method section. The protein concentration used for these measurements is higher (40 µM Tau) relative to the typical concentration used for other experiments, as reported in the main text, to allow for the formation of large condensate volumes, which is favorable for tracking a higher number of fluorescent tracers for nanorheology measurements. To determine the mean-squared displacements of the tracers, the Trackmate[106] plugin of Fiji was used.

The acquired trajectories were subjected to correction for potential drift by subtracting from the center of mass (COM) trajectory, which was estimated using particle velocity as shown below:

$$\boldsymbol{X_{COM}}(k) = \boldsymbol{X_0} + \sum_{j=0}^{k} \frac{1}{N_j} \sum_{i=1}^{N} \boldsymbol{v_{i,j}} \tag{2}$$

Here, k represents the frame number at which $\boldsymbol{X_{COM}}$ is calculated, j represents the individual frame, and N_j represents the number of particles in frame j. $\boldsymbol{X_0}$ represents the center of the mass vector of the first frame. Subsequently, after the correction of the trajectories for drifting, the mean squared displacement (MSD) is estimated as follows:

$$MSD(\tau) = \left\langle \boldsymbol{R}(t+\tau) - \boldsymbol{R}(t) \right\rangle_{t,N} \tag{3}$$

Here, τ represents the lag time and $\boldsymbol{R}$ represents the position vector of the particle. Utilizing various lag times τ, the MSD was estimated based on the trajectories of the particles, with the use of in-house made Python scripts, which are publicly available (*see* 'Code Availability' section). Next, the ensemble-averaged MSD was estimated using measurements from approximately 20–100 individual probe particles. Fitting of the MSD[7,98] was accomplished using:

$$MSD(\tau) = 4D\tau^{\alpha} + N \tag{4}$$

Here, D represents the diffusion coefficient of the particles and α represents the diffusivity exponent, which signifies the nature of the particle diffusion (normal or sub-diffusive) inside the condensates.

With each sample, about 20 to 100 trajectories were acquired from 3 condensates across three independently prepared samples. In order to deduce the condensate aging dynamics either in the presence or absence of small molecules (L-Arg or L-Glu), VPT nanorheology was conducted at two distinct time points during physical aging.

Estimation of dynamical moduli from nanorheology measurements

The viscoelastic properties of Tau condensates were estimated from the MSD measurements, utilizing in-house developed Python scripts (refer to 'Code Availability' section). The protocol followed to estimate the dynamical moduli from MSDs is described in a previous report[9]. In brief, the compliance $j(t)$ was calculated from the MSDs $<\Delta r^2(\tau)>$ estimated from VPT nanorheology measurements described in the previous section using the following equation:

$$j(t) = \frac{3\pi a}{n_d k_B T} <\Delta r^2(\tau)> \tag{5}$$

Here, a represents the probe particle radius, $n_d = 2$ represents the dimension of the probe particle trajectories based on which the MSDs were estimated, k_B represents the Boltzmann constant, and T represents the absolute temperature at which VPT nanorheology experiments were done.

The complex shear modulus can be estimated using a Fourier transform, which relates the complex shear modulus and the compliance via a convolution integral, as shown below:

$$\int_0^{\tau} G(t) j(\tau - t) dt = \tau \tag{6}$$

$$G^*(\omega) = \frac{1}{i\omega \hat{j}(\omega)}. \tag{7}$$

Following the methodology proposed by Evans, R. et al.[107], the complex shear modulus was estimated. Using discrete experimental data points (t_i, j_i) of the estimated compliance from Eq. (5), the frequency-space shear modulus $G^*(\omega)$ is estimated following the equation below:

$$\frac{i\omega}{G^*(\omega)} = i\omega J(0) + \frac{(1 - e^{-i\omega t_1})(J_1 - J(0))}{t_1} + \frac{e^{-i\omega t_N}}{\eta} + \sum_{k=2}^{N} \left(\frac{J_k - J_{k-1}}{t_k - t_{k-1}} \right) \left(e^{-i\omega t_{k-1}} - e^{-i\omega t_k} \right) \tag{8}$$

The MSD data were oversampled using a cubic spline. The remainder of the parameters required in Eq. (8) for estimating the shear modulus can be acquired as follows. $j(0)$ is acquired through extrapolation of the experimental data for compliance $t = 0$ using a linear fit of the initial four data points and η using a linear fit of the final ten data points following the relation, $\eta = 1/\dot{j}(t)$.

Estimation of dense phase area fraction

Confocal fluorescence images visualized with Atto488-labeled SynTag-Tau were used as input for dense phase area fraction estimation. The imaging was conducted after all condensates had settled on the coverslip. Random frames were imaged to ensure an accurate representation of the area fraction. For quantification, thresholding was performed using Fiji in order to isolate condensates from the background (dilute phase), yielding a binarized image highlighting the areas occupied by condensates. Using the 'Analyze Particles' function of Fiji, individual condensate sizes (µm^2) were determined. Subsequently, the fraction of cumulative area occupied by condensates with respect to the total area of image acquisition, set by image acquisition parameters, was estimated. The dense phase area fraction estimations were conducted at different conditions, including varying buffer ionic strength or small molecule concentrations, to assess their impact on phase separation.

Coverslip treatment for microscopy

The experiments of this study used Tween20-coated coverslips. The coverslip cleaning procedure prior to surface coating involves treatment with 2% Hellmanex solution for 2 h, followed by rinsing with MilliQ water six times. Subsequently, coverslips were treated with 20% Tween 20 solution (v/v) for 30 min. Further, these coverslips were rinsed with MilliQ six times and dried with compressed air. Lastly, the coverslips were dried in an oven at 40 °C overnight. The coverslips were later stored at room temperature for use in experiments.

Software

Fiji[96] (version 1.54 f) was used for processing and analyzing microscopy images. A custom Python script was used to plot VPT nanorheology data and estimate dynamical moduli. The scripts are available publicly (*see* 'Code Availability' section). Trackmate (v7.14) was used for nanorheology-related analysis. For all other plots, GraphPad Prism 10 (v10.4.1) was used. MarvinSketch (ChemAxon) was used to visualize the chemical structures of small molecules. Adobe Illustrator (2024) was used for preparing figures and schematics. Igor Pro 8.4 was used for BCARS data processing. Bluelake (v1.6.11) was used for collecting fluorescence

images as well as for performing FRAP and optical tweezer-induced condensate fusion measurements with the Lumicks C-Trap microscope. ZEN (SP5 2012 Black) was used to acquire fluorescence images with the LSM 710 laser-scanning confocal microscope. VistaVision (v4.2) was used to acquire fluorescence images and FLIM measurements with the ISS Q2 laser-scanning confocal microscope. Fusion Dragonfly software (v2.6) was used for acquiring fluorescence images with the Andor Dragonfly 600 confocal platform. UCSF ChimeraX[108] (v1.7) was used for visualizing AlphaFold3[68] predicted structures of Tau protein variants. ZipperDB was used for estimating fibrillization propensity scores[70]. DrugBank was used to generate predicted pK_a values for small molecules[109]. PLAAC[110] was used to generate prion scores of protein variants.

Reporting summary

Further information on research design is available in the Nature Portfolio Reporting Summary linked to this article.

Data availability

Unless otherwise stated, all data supporting the results of this study can be found in the article, supplementary, and source data files. The microscopy imaging data supporting the findings of this study are available in the Dryad Repository[111] under the [https://doi.org/10.5061/dryad.n8pk0p38v]. Source data are provided with this paper.

Code availability

The codes for nanorheology-related analyses are available on Zenodo[112] under the [https://doi.org/10.5281/zenodo.18088578].

References

1. Martin, E. W. et al. Valence and patterning of aromatic residues determine the phase behavior of prion-like domains. *Science* **367**, 694–699 (2020).
2. Ginell G. M., Holehouse A. S. An Introduction to the Stickers-and-Spacers Framework as Applied to Biomolecular Condensates. In: Zhou H.-X., Spille J.-H., Banerjee P. R. (eds). *Phase-Separated Biomolecular Condensates: Methods and Protocols*. Springer US: New York, NY, pp 95–116 (2023).
3. Pappu, R. V., Cohen, S. R., Dar, F., Farag, M. & Kar, M. Phase transitions of associative biomacromolecules. *Chem. Rev.* **123**, 8945–8987 (2023).
4. Dignon, G. L., Best, R. B. & Mittal, J. Biomolecular phase separation: from molecular driving forces to macroscopic properties. *Annu. Rev. Phys. Chem.* **71**, 53–75 (2020).
5. Rekhi, S. et al. Expanding the molecular language of protein liquid–liquid phase separation. *Nat. Chem.* **16**, 1113–1124 (2024).
6. Brangwynne, C. P. et al. Germline P granules are liquid droplets that localize by controlled dissolution/condensation. *Science* **324**, 1729–1732 (2009).
7. Alshareedah, I., Moosa, M. M., Pham, M., Potoyan, D. A. & Banerjee, P. R. Programmable viscoelasticity in protein-RNA condensates with disordered sticker-spacer polypeptides. *Nat. Commun.* **12**, 1–14 (2021).
8. Jawerth, L. et al. Protein condensates as aging Maxwell fluids. *Science* **370**, 1317–1323 (2020).
9. Alshareedah, I. et al. Sequence-specific interactions determine viscoelasticity and ageing dynamics of protein condensates. *Nat. Phys.* 10.1101/2023.04.06.535902 (2024).
10. Kato, M. et al. Cell-free formation of RNA granules: low complexity sequence domains form dynamic fibers within hydrogels. *Cell* **149**, 753–767 (2012).
11. Molliex, A. et al. Phase separation by low complexity domains promotes stress granule assembly and drives pathological fibrillization. *Cell* **163**, 123–133 (2015).
12. Patel, A. et al. A liquid-to-solid phase transition of the als protein fus accelerated by disease mutation. *Cell* **162**, 1066–1077 (2015).
13. St George-Hyslop, P. et al. The physiological and pathological biophysics of phase separation and gelation of RNA binding proteins in amyotrophic lateral sclerosis and fronto-temporal lobar degeneration. *Brain Res* **1693**, 11–23 (2018).
14. Lin, Y., Protter, D. S., Rosen, M. K. & Parker, R. Formation and maturation of phase-separated liquid droplets by rna-binding proteins. *Mol. Cell* **60**, 208–219 (2015).
15. Zbinden, A., Pérez-Berlanga, M., De Rossi, P. & Polymenidou, M. Phase separation and neurodegenerative diseases: a disturbance in the force. *Dev. Cell* **55**, 45–68 (2020).
16. Murakami, T. et al. ALS/FTD mutation-induced phase transition of fus liquid droplets and reversible hydrogels into irreversible hydrogels impairs rnp granule function. *Neuron* **88**, 678–690 (2015).
17. Linsenmeier, M. et al. The interface of condensates of the hnRNPA1 low-complexity domain promotes formation of amyloid fibrils. *Nat. Chem.* **15**, 1340–1349 (2023).
18. Zhou, X. et al. Mutations linked to neurological disease enhance self-association of low-complexity protein sequences. *Science* **377**, eabn5582 (2022).
19. Alberti, S. & Dormann, D. Liquid–liquid phase separation in disease. *Annu. Rev. Genet.* **53**, 171–194 (2019).
20. Alberti, S. & Carra, S. Quality control of membraneless organelles. *J. Mol. Biol.* **430**, 4711–4729 (2018).
21. Alberti, S., Gladfelter, A. & Mittag, T. Considerations and challenges in studying liquid-liquid phase separation and biomolecular condensates. *Cell* **176**, 419–434 (2019).
22. Alberti, S. & Hyman, A. A. Biomolecular condensates at the nexus of cellular stress, protein aggregation disease and ageing. *Nat. Rev. Mol. Cell Biol.* **22**, 196–213 (2021).
23. Babinchak, W. M. & Surewicz, W. K. Liquid–liquid phase separation and its mechanistic role in pathological protein aggregation. *J. Mol. Biol.* **432**, 1910–1925 (2020).
24. Das, T. et al. Tunable metastability of condensates reconciles their dual roles in amyloid fibril formation. *Mol. Cell* **85**, 2230–2245.e2237 (2025).
25. Zhang, P. et al. Chronic optogenetic induction of stress granules is cytotoxic and reveals the evolution of ALS-FTD pathology. *eLife* **8**, e39578 (2019).
26. Patel, A. et al. ATP as a biological hydrotrope. *Science* **356**, 753–756 (2017).
27. Choi, K.-J. et al. A Chemical Chaperone Decouples TDP-43 Disordered Domain Phase Separation from Fibrillation. *Biochemistry* **57**, 6822–6826 (2018).
28. Qamar, S. et al. FUS phase separation is modulated by a molecular chaperone and methylation of arginine cation-π interactions. *Cell* **173**, 720–734.e715 (2018).
29. Gu, J. et al. Hsp40 proteins phase separate to chaperone the assembly and maintenance of membraneless organelles. *Proc. Natl. Acad. Sci. USA* **117**, 31123–31133 (2020).
30. Linsenmeier, M. et al. Dynamic arrest and aging of biomolecular condensates are modulated by low-complexity domains, RNA and biochemical activity. *Nat. Commun.* **13**, 3030 (2022).
31. Hofweber, M. et al. Phase separation of fus is suppressed by its nuclear import receptor and arginine methylation. *Cell* **173**, 706–719.e713 (2018).
32. Babinchak, W. M. et al. Small molecules as potent biphasic modulators of protein liquid-liquid phase separation. *Nat. Commun.* **11**, 5574 (2020).
33. Wheeler, R. J. et al. Small molecules for modulating protein driven liquid-liquid phase separation in treating neurodegenerative disease. *bioRxiv* 2019: 721001.

34. Freibaum, B. D. et al. Identification of small molecule inhibitors of G3BP-driven stress granule formation. *J. Cell Biol.* **223** (2024).
35. Klein, I. A. et al. Partitioning of cancer therapeutics in nuclear condensates. *Science* **368**, 1386–1392 (2020).
36. Mitrea, D. M., Mittasch, M., Gomes, B. F., Klein, I. A. & Murcko, M. A. Modulating biomolecular condensates: a novel approach to drug discovery. *Nat. Rev. Drug Discov.* **21**, 841–862 (2022).
37. Patel, A. et al. Principles and functions of condensate modifying drugs. *Front Mol. Biosci.* **9**, 1007744 (2022).
38. Dada, S. T. et al. Pharmacological inhibition of α-synuclein aggregation within liquid condensates. *Nat. Commun.* **15**, 3835 (2024).
39. Ambadi Thody, S. et al. Small-molecule properties define partitioning into biomolecular condensates. *Nat. Chem.* **16**, 1794–1802 (2024).
40. Ray, S. et al. α-Synuclein aggregation nucleates through liquid-liquid phase separation. *Nat. Chem.* **12**, 705–716 (2020).
41. Lee, V. M., Goedert, M. & Trojanowski, J. Q. Neurodegenerative tauopathies. *Annu Rev. Neurosci.* **24**, 1121–1159 (2001).
42. Zhang, Y., Wu, K.-M., Yang, L., Dong, Q. & Yu, J.-T. Tauopathies: new perspectives and challenges. *Mol. Neurodegeneration* **17**, 28 (2022).
43. Goedert, M., Eisenberg, D. S. & Crowther, R. A. Propagation of Tau aggregates and neurodegeneration. *Annu. Rev. Neurosci.* **40**, 189–210 (2017).
44. Wang, Y. & Mandelkow, E. Tau in physiology and pathology. *Nat. Rev. Neurosci.* **17**, 22–35 (2016).
45. Götz, J., Halliday, G. & Nisbet, R. M. Molecular pathogenesis of the tauopathies. *Annu Rev. Pathol: Mech. Dis.* **14**, 239–261 (2019).
46. Hernández-Vega, A. et al. Local nucleation of microtubule bundles through tubulin concentration into a condensed Tau phase. *Cell Rep.* **20**, 2304–2312 (2017).
47. Tan, R. et al. Microtubules gate tau condensation to spatially regulate microtubule functions. *Nat. Cell Biol.* **21**, 1078–1085 (2019).
48. Ash, P. E. A. et al. TIA1 potentiates tau phase separation and promotes generation of toxic oligomeric tau. *Proc. Natl. Acad. Sci.* **118**, e2014188118 (2021).
49. Kanaan N. M., Hamel C., Grabinski T., Combs B. Liquid-liquid phase separation induces pathogenic tau conformations in vitro. *Nat. Commun.* **11**, 2809 (2020).
50. Wegmann, S. et al. Tau protein liquid–liquid phase separation can initiate tau aggregation. *The EMBO J*, **37,** 10.1016/j.tcb.2022.01.011 (2018).
51. Boyko, S., Surewicz, K. & Surewicz, W. K. Regulatory mechanisms of tau protein fibrillation under the conditions of liquid–liquid phase separation. *Proc. Natl. Acad. Sci. USA* **117**, 31882–31890 (2020).
52. Hochmair, J. et al. Molecular crowding and RNA synergize to promote phase separation, microtubule interaction, and seeding of Tau condensates. *EMBO J*, e108882 (2022).
53. Meisl, G., Knowles, T. P. J. & Klenerman, D. Mechanistic Models of Protein Aggregation Across Length-Scales and Time-Scales: From the Test Tube to Neurodegenerative Disease. *Front Neurosci.* **16**, 909861 (2022).
54. Meisl, G. et al. In vivo rate-determining steps of tau seed accumulation in Alzheimer's disease. *Sci. Adv.* **7**, eabh1448 (2021).
55. Mandelkow, E.-M. & Mandelkow, E. Biochemistry and cell biology of tau protein in neurofibrillary degeneration. *Cold Spring Harb. Perspect. Med.* **2**, a006247 (2012).
56. Lin, Y., Fichou, Y., Zeng, Z., Hu, N. Y. & Han, S. Electrostatically driven complex coacervation and amyloid aggregation of tau are independent processes with overlapping conditions. *ACS Chem. Neurosci.* **11**, 615–627 (2020).
57. Huang, Y. et al. Methylene blue accelerates liquid-to-gel transition of tau condensates impacting tau function and pathology. *Nat. Commun.* **14**, 5444 (2023).
58. Savastano, A. et al. Disease-associated tau phosphorylation hinders tubulin assembly within tau condensates. *Angew. Chem. Int Ed.* **60**, 726–730 (2021).
59. Chuang, H.-Y. et al. Engineered droplet-forming peptide as photocontrollable phase modulator for fused in sarcoma protein. *Nat. Commun.* **15**, 5686 (2024).
60. Piroska, L. et al. α-Synuclein liquid condensates fuel fibrillar α-synuclein growth. *Sci. Adv.* **9**, eadg5663 (2023).
61. Khan, T. et al. Quantifying nucleation in vivo reveals the physical basis of prion-like phase behavior. *Mol. Cell* **71**, 155–168.e157 (2018).
62. Goehler, H. et al. Pathogenic polyglutamine tracts are potent inducers of spontaneous sup35 and rnq1 amyloidogenesis. *PLoS One* **5**, e9642 (2010).
63. Chandramowlishwaran, P. et al. Mammalian amyloidogenic proteins promote prion nucleation in yeast. *J. Biol. Chem.* **293**, 3436–3450 (2018).
64. Toombs, J. A. et al. De novo design of synthetic prion domains. *Proc. Natl. Acad. Sci. USA* **109**, 6519–6524 (2012).
65. Michiels, E. et al. Entropic bristles tune the seeding efficiency of prion-nucleating fragments. *Cell Rep.* **30**, 2834–2845.e2833 (2020).
66. Alberti, S., Halfmann, R., King, O., Kapila, A. & Lindquist, S. A systematic survey identifies prions and illuminates sequence features of prionogenic proteins. *Cell* **137**, 146–158 (2009).
67. Halfmann, R. et al. Opposing effects of glutamine and asparagine govern prion formation by intrinsically disordered proteins. *Mol. Cell* **43**, 72–84 (2011).
68. Abramson, J. et al. Accurate structure prediction of biomolecular interactions with AlphaFold 3. *Nature* **630**, 493–500 (2024).
69. Mahendran, T. S. et al. Viscoelasticity and interface properties of multi-component condensates govern protein sequestration and suppression of amyloid formation. *bioRxiv* 2025**:** 2025.2012.2029.695806.
70. Goldschmidt, L., Teng, P. K., Riek, R. & Eisenberg, D. Identifying the amylome, proteins capable of forming amyloid-like fibrils. *Proc. Natl. Acad. Sci. USA* **107**, 3487–3492 (2010).
71. Jennings, C. M. et al. Collagen organization and structure in FBLN5-/- mice using label-free microscopy: implications for pelvic organ prolapse. *Biomed. Opt. Express* **15**, 2863–2875 (2024).
72. Kwan, A. C., Duff, K., Gouras, G. K. & Webb, W. W. Optical visualization of Alzheimer's pathology via multiphoton-excited intrinsic fluorescence and second harmonic generation. *Opt. Express* **17**, 3679–3689 (2009).
73. Chatterjee, S. et al. Reversible kinetic trapping of fus biomolecular condensates. *Adv. Sci.* **9**, 2104247 (2022).
74. Najafi, S. et al. Liquid–liquid phase separation of Tau by self and complex coacervation. *Protein Sci.* **30**, 1393–1407 (2021).
75. Ukmar-Godec, T. et al. Lysine/RNA-interactions drive and regulate biomolecular condensation. *Nat. Commun.* **10**, 1–15 (2019).
76. Kaur, T. et al. Molecular Crowding Tunes Material States Of Ribonucleoprotein Condensates. *Biomolecules* **9**, 71 (2019).
77. Wei, M.-T. et al. Phase behaviour of disordered proteins underlying low density and high permeability of liquid organelles. *Nat. Chem.* **9**, 1118–1125 (2017).
78. Takarai, H., Yasuda, T., Sakumichi, N. & Sakai, T. Partitioning Law of Polymer Chains into Flexible Polymer Networks. *arXiv preprint arXiv:250505254* 2025.
79. Emmanouilidis, L. et al. A solid beta-sheet structure is formed at the surface of FUS droplets during aging. *Nat. Chem. Biol.* **20**, 1044–1052 (2024).

80. Shen, Y. et al. The liquid-to-solid transition of FUS is promoted by the condensate surface. *Proc. Natl. Acad. Sci. USA* **120**, e2301366120 (2023).
81. Farag, M. et al. Condensates formed by prion-like low-complexity domains have small-world network structures and interfaces defined by expanded conformations. *Nat. Commun.* **13**, 7722 (2022).
82. Ruff, K. M., Dar, F. & Pappu, R. V. Polyphasic linkage and the impact of ligand binding on the regulation of biomolecular condensates. *Biophys. Rev. (Melville)* **2**, 021302 (2021).
83. Mathieu, C., Pappu, R. V. & Taylor, J. P. Beyond aggregation: Pathological phase transitions in neurodegenerative disease. *Science* **370**, 56–60 (2020).
84. Mahendran, T. S., Wadsworth, G. M., Singh, A., Gupta, R. & Banerjee, P. R. Homotypic RNA clustering accompanies a liquid-to-solid transition inside the core of multi-component biomolecular condensates. *Nat. Chem.* **17**, 1236–1246 (2025).
85. Joshi, M. S. et al. Receptor-mediated activation of nitric oxide synthesis by arginine in endothelial cells. *Proc. Natl. Acad. Sci.* **104**, 9982–9987 (2007).
86. Baydoun, A. R., Emery, P. W., Pearson, J. D. & Mann, G. E. Substrate-dependent regulation of intracellular amino acid concentrations in cultured bovine aortic endothelial cells. *Biochem Biophys. Res Commun.* **173**, 940–948 (1990).
87. Mittag, T. & Pappu, R. V. A conceptual framework for understanding phase separation and addressing open questions and challenges. *Mol. Cell* **82**, 2201–2214 (2022).
88. Harmon, T. S., Holehouse, A. S., Rosen, M. K. & Pappu, R. V. Intrinsically disordered linkers determine the interplay between phase separation and gelation in multivalent proteins. *eLife* **6**, e30294 (2017).
89. Boeynaems, S. et al. Protein phase separation: a new phase in cell biology. *Trends Cell Biol.* **28**, 420–435 (2018).
90. Lipiński, W. P. et al. Biomolecular condensates can both accelerate and suppress aggregation of α-synuclein. *Sci. Adv.* **8**, eabq6495 (2022).
91. Li, Y. R., King, O. D., Shorter, J. & Gitler, A. D. Stress granules as crucibles of ALS pathogenesis. *J. Cell Biol.* **201**, 361–372 (2013).
92. Biswas, S. & Potoyan, D. A. Molecular drivers of aging in biomolecular condensates: desolvation, rigidification, and sticker lifetimes. *PRX Life* **2**, 023011 (2024).
93. Wang, L., Bharti, Kumar, R., Pavlov, P. F. & Winblad, B. Small molecule therapeutics for tauopathy in Alzheimer's disease: Walking on the path of most resistance. *Eur. J. Medicinal Chem.* **209**, 112915 (2021).
94. Garcia-Cabau, C. et al. Mis-splicing of a neuronal microexon promotes CPEB4 aggregation in ASD. *Nature* **637**, 496–503 (2025).
95. Wake, N. et al. Expanding the molecular grammar of polar residues and arginine in FUS phase separation. *Nat. Chem. Biol.* **21**, 1076–1088 (2025).
96. Schindelin, J. et al. Fiji: an open-source platform for biological-image analysis. *Nat. Methods* **9**, 676–682 (2012).
97. Alshareedah I., Kaur T., Banerjee P. R. Chapter Six - Methods for characterizing the material properties of biomolecular condensates. In: Keating C. D. (ed). *Methods in Enzymology*, vol. 646. Academic Press, 143–183 (2021).
98. Alshareedah, I., Thurston, G. M. & Banerjee, P. R. Quantifying viscosity and surface tension of multicomponent protein-nucleic acid condensates. *Biophys. J.* **120**, 1161–1169 (2021).
99. Ghosh, A., Kota, D. & Zhou, H. X. Determining thermodynamic and material properties of biomolecular condensates by confocal microscopy and optical tweezers. *Methods Mol. Biol.* **2563**, 237–260 (2023).
100. Parekh, S. H., Lee, Y. J., Aamer, K. A. & Cicerone, M. T. Label-free cellular imaging by broadband coherent anti-Stokes Raman scattering microscopy. *Biophys. J.* **99**, 2695–2704 (2010).
101. Liu, Y., Lee, Y. J. & Cicerone, M. T. Broadband CARS spectral phase retrieval using a time-domain Kramers–Kronig transform. *Opt. Lett.* **34**, 1363–1365 (2009).
102. Movasaghi, Z., Rehman, S. & Rehman, I. U. Raman spectroscopy of biological tissues. *Appl. Spectrosc. Rev.* **42**, 493–541 (2007).
103. Fleissner, F., Bonn, M. & Parekh, S. H. Microscale spatial heterogeneity of protein structural transitions in fibrin matrices. *Sci. Adv.* **2**, e1501778 (2016).
104. Berjot, M., Marx, J. & Alix, A. J. P. Determination of the secondary structure of proteins from the Raman amide I band: The reference intensity profiles method. *J. Raman Spectrosc.* **18**, 289–300 (1987).
105. Quan, M. D., Liao, S. J., Ferreon, J. C. & Ferreon, A. C. M. Fluorescence lifetime imaging microscopy of biomolecular condensates. *Methods Mol. Biol.* **2563**, 135–148 (2023).
106. Tinevez, J.-Y. et al. TrackMate: An open and extensible platform for single-particle tracking. *Methods (San. Diego, Calif.)* **115**, 80–90 (2017).
107. Evans, R., Tassieri, M., Auhl, D. & Waigh, T. A. Direct conversion of rheological compliance measurements into storage and loss moduli. *Phys. Rev. E* **80**, 012501 (2009).
108. Meng, E. C. et al. UCSF ChimeraX: Tools for structure building and analysis. *Protein Sci.* **32**, e4792 (2023).
109. Knox, C. et al. DrugBank 6.0: the DrugBank Knowledgebase for 2024. *Nucleic Acids Res* **52**, D1265–d1275 (2024).
110. Lancaster, A. K., Nutter-Upham, A., Lindquist, S. & King, O. D. PLAAC: a web and command-line application to identify proteins with prion-like amino acid composition. *Bioinformatics* **30**, 2501–2502 (2014).
111. Mahendran T. S. et al. Decoupling Phase Separation and Fibrillization Preserves Activity of Biomolecular Condensates. Dryad 2025. https://doi.org/10.5061/dryad.n8pk0p38v.
112. Mahendran T. S. et al. Decoupling Phase Separation and Fibrillization Preserves Activity of Biomolecular Condensates. Zenodo 2025. https://doi.org/10.5281/zenodo.18088578.

Acknowledgements

This work was supported by the US National Institutes of Health (NIH) through grants R03 AG070510 (to P.R.B.), R35 GM138186 (to P.R.B.), and the St. Jude Children's Research Collaborative on the Biology and Biophysics of RNP Granules (to P.R.B.). We are grateful for financial support from the Welch Foundation (F-2008-20220331), the Chan Zuckerberg Initiative (#2021-236087), and the National Science Foundation (NSF) (#2146549) to S.H.P., and C.M.J. is grateful for support from NSF (DGE-1610403) and NIH T32 EB007507. We would like to gratefully acknowledge Dr. Ibraheem Alshareedah, currently at Los Alamos National Laboratory, and Paul Dewan, currently at Harvard University, for their technical support during the study's development phase. Also, the authors greatly appreciate the critical feedback from the Banerjee laboratory group members and from Drs. R. Pappu and T. Mittag. Any opinions, findings, conclusions, or recommendations expressed in this material are those of the author(s) and do not necessarily reflect the views of the NSF, NIH, or any other bodies.

Author contributions

Conceptualization: P.R.B. and T.S.M. Methodology: P.R.B., T.S.M., A.S., S.S., S.H.P., C.M.J., C.N., and B.H.G. Investigation: P.R.B., T.S.M., A.S., S.S., S.H.P., and C.M.J. Data curation: P.R.B., T.S.M., A.S., S.H.P., and C.M.J. Formal analysis: P.R.B., T.S.M., A.S., S.H.P., and C.M.J. Visualization: P.R.B., T.S.M., A.S., S.H.P., and C.M.J. Writing – original draft: P.R.B. and T.S.M. Writing – review & editing: P.R.B., T.S.M., A.S., S.S., S.H.P., and C.M.J. Supervision: P.R.B. Funding acquisition: P.R.B. and S.H.P.

Competing interests

P.R.B. is a member of the Biophysics Reviews (AIP Publishing) editorial board. This affiliation did not influence the work reported here. The remaining authors declare no competing interests.

Additional information

Supplementary information The online version contains supplementary material available at https://doi.org/10.1038/s41467-026-69244-z.

Correspondence and requests for materials should be addressed to Priya R. Banerjee.

Peer review information *Nature Communications* thanks the anonymous reviewers for their contribution to the peer review of this work. A peer review file is available.